Remote sensing proxies underestimate fire-induced gross primary productivity loss and overestimate recovery in forests

Xinyi Fan [a,b], Qinggaozi Zhu [c], Yingnan Wei [a,b], Ning Yao [d,e], Gang Zhao [a,b], Qiang Yu [b,*], Genghong Wu [a,b,*]

[a] College of Soil and Water Conservation Science and Engineering, Northwest A&F University, Yangling, Shaanxi, 712100, China
[b] State Key Laboratory of Soil and Water Conservation and Desertification Control, Institute of Soil and Water Conservation Northwest A&F University, Yangling, Shaanxi, 712100, China
[c] New South Wales Department of Climate Change, Energy, the Environment and Water, Parramatta, New South Wales, Australia
[d] College of Water Resources and Architectural Engineering, Northwest A&F University, Yangling, Shaanxi, 712100, China
[e] Key Lab of Agricultural Water and Soil Engineering of Education Ministry, Northwest A&F University, Yangling, Shaanxi, 712100, China

ARTICLE INFO

ABSTRACT

Wildfires significantly alter terrestrial carbon cycling by reducing vegetation productivity and reshaping ecosystem functioning, yet satellite-based estimates of gross primary productivity (GPP) remain highly uncertain under fire disturbance. Here, we evaluated five global GPP products—BESS GPP (process-based), FLUXCOM and FluxSat GPP (machine learning-based), GOSIF GPP (derived from reconstructed solar-induced chlorophyll fluorescence, SIF), MODIS GPP (light-use efficiency–based)—together with three complementary proxies: GOSIF (reconstructed SIF), the near-infrared reflectance of vegetation (NIRv), and leaf area index (LAI). These products were benchmarked against eddy covariance (EC) tower GPP measurements from ten fire-affected sites (five forest sites, five grass/shrub sites) with multi-year pre- and post-fire records. Results show that satellite proxies generally underestimated fire-induced GPP loss, with forest sites showing the largest discrepancy: EC GPP declined by ~94%, compared to 47–88% from satellites. During recovery, most satellite products overestimated post-fire carbon gain and underestimated recovery time, often signaling premature recovery in forests. In contrast, grass and shrub ecosystems showed faster rebound and closer agreement with satellite estimates. Among these products, BESS GPP and GOSIF better reproduced immediate loss and recovery time, though still underestimated persistent suppression and overestimated cumulative uptake. Moreover, EC data further revealed reduced post-fire GPP sensitivity to light, temperature, and vapor pressure deficit in forests, which satellite products failed to capture. These findings highlight systematic biases in current satellite proxies, emphasize the challenges in monitoring forest recovery, and underscore the need for disturbance-responsive models and expanded flux benchmarks to improve post-fire carbon cycle assessments.

1. Introduction

Wildfire is a major disturbance in terrestrial ecosystems, profoundly affecting vegetation structure, productivity, and biogeochemical cycles (Lv et al., 2025; Xu et al., 2024). In recent years, intensified global warming has increased the frequency of extreme heat and drought events, prolonging fire seasons and amplifying fire severity (Flannigan et al., 2013). Between 2001 and 2020, the global average annual burned area (BA) was approximately 7.74×10^6 km² (Chen et al., 2023). Although the overall global BA declined, high-intensity and large-scale wildfire events have continued to rise in key regions such as Canada,

Siberia, and Australia (Andela et al., 2017; Canadell et al., 2021; Gui et al., 2025; Huang et al., 2024; Jones et al., 2024). These disturbances can result in immediate vegetation mortality and trigger long-term ecosystem shifts (Xu et al. 2025; Zhou et al. 2023), with cascading impacts on the carbon cycle (Burton et al., 2024; Hung et al., 2024; Walker et al., 2019), hydrology (Baur et al., 2024; Shakesby and Doerr, 2006; Wine and Cadol, 2016), and land-atmosphere interactions (Tian et al., 2022; Zhao et al., 2024). Accurately quantifying the magnitude and trajectory of post-fire ecosystem recovery is essential for understanding terrestrial carbon dynamics and for improving climate-biosphere feedback models.

Earth observation (EO) remote sensing has become an essential tool for monitoring post-disturbance vegetation dynamics, owing to its broad spatial coverage and increasing availability of long-term datasets (Runge et al., 2025; Wooster et al., 2021). Among various satellite-derived indicators, gross primary production (GPP) is widely recognized as a functionally meaningful metric for assessing productivity loss and recovery after fire (Huang et al., 2013; Sun et al., 2020; Xu et al., 2024). Because GPP cannot be directly measured from space, current satellite GPP products are mostly generated through models that integrate satellite observations (e.g., surface reflectance, vegetation indices) with meteorological data (Prentice et al., 2024; Ryu et al., 2019; Wang et al., 2025; Xiao et al., 2019). These products can be broadly classified into three methodological categories: (1) Process-based models, such as the Breathing Earth System Simulator (BESS) and the Boreal Ecosystem Productivity Simulator (BEPS), which explicitly simulate canopy photosynthesis and energy fluxes by coupling radiative transfer, biochemical, and biophysical processes (Jiang and Ryu, 2016; Liu et al., 1997); (2) Machine learning approaches, which empirically learn relationships between satellite predictors and in situ GPP from eddy covariance (EC) towers, including FLUXCOM and FluxSat (Joiner et al., 2018; Jung et al., 2020; Nelson et al., 2024); and (3) Light use efficiency (LUE) models, such as MODIS GPP (MOD17) and the Vegetation Photosynthesis Model (VPM), which estimate GPP as the product of absorbed photosynthetically active radiation (APAR), maximum LUE, and downregulating scalars representing environmental stress (e.g., temperature, vapor pressure deficit) (Haxeltine and Prentice, 1996; Running et al., 2004; Zhang et al., 2017). These GPP products have been widely applied to quantify post-fire reductions in ecosystem productivity (Bandopadhyay and Sánchez, 2020; Wu et al., 2024; Zong et al., 2024), to evaluate the magnitude and duration of fire-induced declines (Kelly et al., 2024; Lv et al., 2025; Xu et al., 2024), and to characterize long-term recovery trajectories across diverse biomes (Gu et al., 2025; Hemes et al., 2023; Sun et al., 2020; Ueyama et al., 2019).

In parallel, solar-induced chlorophyll fluorescence (SIF) has emerged as a direct optical proxy of photosynthetic activity, offering an alternative pathway for GPP estimation (Frankenberg et al., 2011; Ryu et al., 2019). SIF-based products such as GOSIF GPP generate spatially continuous GPP estimates through biome-specific empirical scaling of reconstructed OCO-2 SIF observations (Li et al. 2019a). Beyond its role in GPP estimation, SIF—whether from original satellite retrievals, spatially reconstructed datasets (e.g., GOSIF), or downscaled products—has proven valuable for detecting fire-induced vegetation stress, tracking recovery trajectories, and identifying the timing of photosynthetic rebound (Guo et al., 2021; Kim et al., 2024; Shen et al., 2025). Complementing these functional indicators, structural and spectral proxies such as leaf area index (LAI) and near-infrared reflectance of vegetation (NIRv) have been widely used to capture post-fire canopy defoliation and regrowth dynamics (Badgley et al. 2017; Zhou et al. 2025). NIRv, in particular, effectively isolates vegetation signals from soil background and has demonstrated strong correlation with GPP across biomes (Badgley et al., 2019). Classic vegetation indices such as normalized difference vegetation index (NDVI) and enhanced vegetation index (EVI) continue to serve as simple yet informative indicators of fire-induced changes in greenness and canopy structure (Ba et al., 2022; Gülci and Wing, 2025; Singh and Jeganathan, 2023; Srivastava et al., 2025). The combination of functional indicators (e.g., GPP, SIF) and structural metrics (e.g., LAI, NIRv, EVI) provides a more comprehensive assessment of fire impacts and post-disturbance ecosystem recovery pathways.

Although a wide range of satellite GPP products and vegetation proxies have been used to assess fire-induced carbon loss and post-fire recovery, the choice of products varies considerably across studies (Bastos et al., 2011; Fan et al., 2023; Hemes et al., 2023; Pan et al., 2025; Xu et al., 2024), and few have been systematically validated against in situ measurements such as EC fluxes across different ecosystems. This lack of benchmarking limits the comparability and interpretability of results, particularly when extrapolated to regional or global scales. For instance, Hemes et al. (2023) combined Landsat-derived NIRv with EC data in Californian forests, reporting sharp GPP declines post-fire, with full recovery taking over a decade in severely burned areas. In contrast, Pan et al. (2025) found rapid GPP recovery in Australian savannas and woodlands using multiple satellite products, including MODIS, VPM, BESS, and GOSIF GPP, with most sites recovering to or exceeding pre-fire productivity within two years. Xu et al. (2024) conducted a global assessment based on GOSIF GPP and vegetation indices, revealing biome-specific recovery patterns—rapid in grasslands and shrublands, but substantially delayed in evergreen forests. At the site scale, Woodgate et al. (2025) observed post-fire mismatches between satellite-derived SIF and EC-based GPP in an Australian eucalypt forest, where satellite proxies underestimated recovery duration. Collectively, these studies highlight the inconsistency in recovery trajectories across products and ecosystems, underscoring the need for systematic, cross-product validation using EC benchmarks. Furthermore, the ability of satellite products to capture post-fire shifts in GPP sensitivity to environmental drivers—such as light, temperature, and vapor pressure deficit (VPD)—remains insufficiently tested, especially in forest systems where canopy damage may alter land–atmosphere coupling.

To address these gaps, we systematically evaluate multiple remote sensing proxies—including five global GPP products (BESS, FLUXCOM, FluxSat, GOSIF and MODIS GPP) and three complementary proxies (SIF, NIRv, and LAI)—against EC-derived GPP across ten fire-affected sites (five forest sites and five grass/shrub sites). Specifically, we assess their capacity to capture fire-induced GPP loss, post-fire GPP accumulation, time to recovery, and recovery rate, as well as their ability to reproduce observed shifts in GPP sensitivity to meteorological drivers before and after fire. This study focuses on sites in Australia and North America, representing two major fire-prone regions of the Southern and Northern Hemispheres (Bradstock, 2010; Phillips et al., 2022; Schoennagel et al., 2017; Williams et al., 2012). These regions offer a diverse range of fire-impacted ecosystems, from forests to grasslands and shrublands, and are equipped with extensive EC measurements (Baldocchi et al., 2024; Beringer et al., 2016), making them ideal for systematically benchmarking satellite products. Integrating EC flux observations with multiple remote sensing proxies enables a comprehensive assessment of wildfire impacts and post-fire recovery across distinct ecosystems. Building on this foundation, our study introduces a evaluation framework that combines functional and structural indicators to clarify the mechanisms underlying satellite–EC discrepancies. This integrative, cross-ecosystem benchmark represents the first coordinated evaluation of major global GPP products in fire-affected forests and grass/shrub systems, providing clearer guidance for selecting robust proxies and informing the development of next-generation satellite products.

2. Data and methods

2.1. Eddy covariance flux data

We selected ten EC tower sites from the OzFlux and AmeriFlux networks that provide multi-year, continuous observations spanning both pre-fire and post-fire periods (Fig. 1; Table 1). These sites represent the limited set of globally available locations with publicly accessible flux records covering the full fire disturbance timeline. Of the ten, four were in Australia (AU-Wac, AU-Cpr, AU-Tum, AU-Wrr) and six in the United States (US-Vcm, US-Me2, US-Seg, US-Scg, US-Scs, US-SO2), collectively encompassing a variety of ecosystems including evergreen needleleaf and broadleaf forests, shrublands, grasslands, and savannas. Based on the relative differenced Normalized Burn Ratio (RdNBR) method (Miller and Thode, 2007; Pan et al., 2025), we classified fire severity at all sites using established thresholds: low severity (RdNBR < 0.4), moderate severity (0.4 ≤ RdNBR ≤ 0.8), and high severity (RdNBR > 0.8). The results (Fig. S1) indicate that AU-Tum, AU-Wac, US-Scg, and US-Scs experienced moderate-severity fires, while all other sites were affected
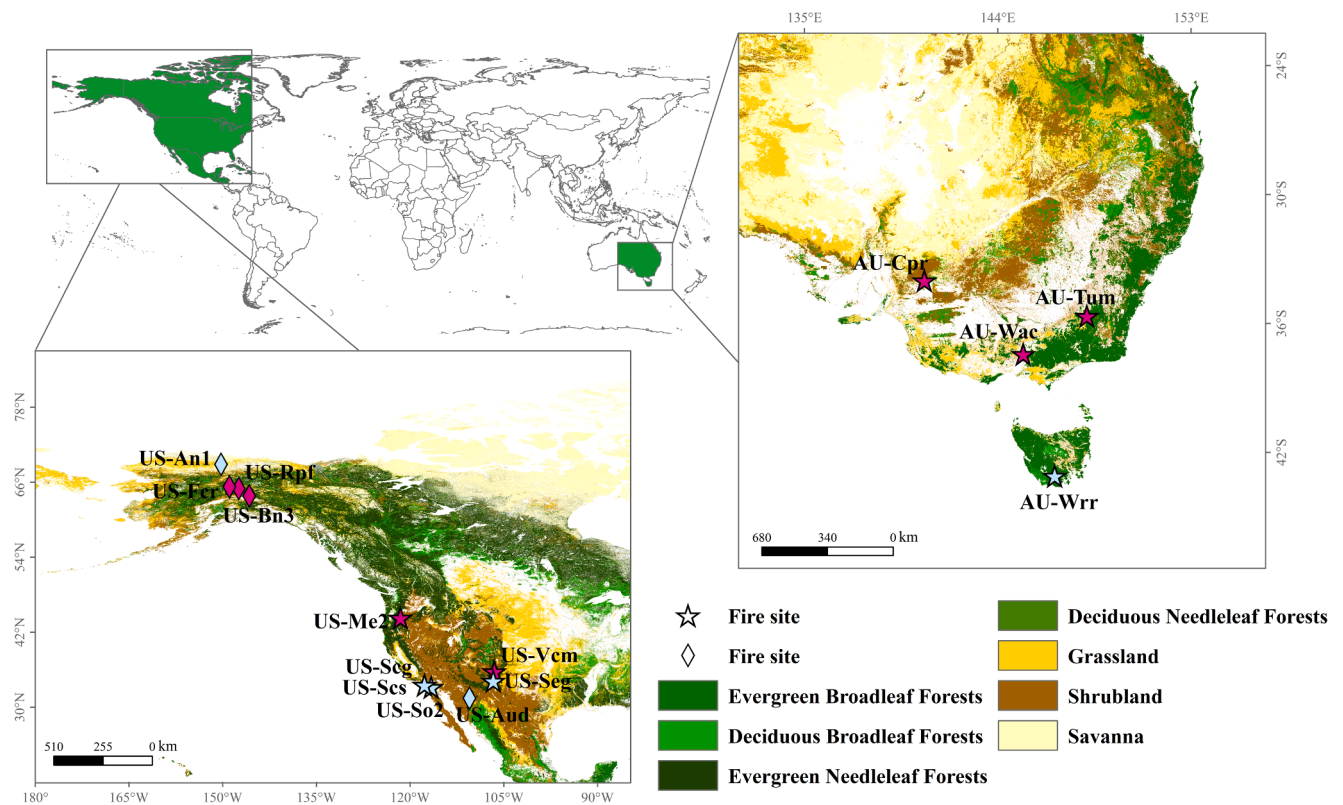
Fig. 1. Geographic distribution of eddy covariance flux tower sites used in this study. Stars represent sites with observational records spanning the pre- and post-fire periods, while diamonds denote sites where observations began within five years after the fire event. Sites are color-coded by the dominant fire-affected vegetation type: magenta for forest-dominated sites, and blue for grass, shrub, or understory-dominated sites. The AU-Cpr site is classified as forest following Sun et al. (2020).

Table 1

Overview of the eddy covariance flux tower sites with observational records spanning the pre- and post-fire period. For each site, the fire event date, geographic coordinates, pre-fire dominant plant functional type (based on IGBP classification), data coverage period, and data source (OzFlux or AmeriFlux) are listed.

Site ID	Site Name	Fire Event	Lon, Lat	Pre-fire plant functional type	Data Coverage	Database
AU-Cpr	Calperum Chowilla	2014/01	140.59°E, 34.00°S	Savannas	2010–2024	OzFlux
AU-Tum	Tumbarumba	2019/12	148.15°E, 35.66°S	Evergreen Broadleaf Forests	2002–2022	OzFlux
AU-Wac	Wallaby Creek	2009/02	145.19°E, 37.43°S	Evergreen Broadleaf Forests	2005–2013	OzFlux
AU-Wrr	Warra	2019/01	146.65°E, 43.10°S	Evergreen Broadleaf Forests	2013–2021	OzFlux
US-Vcm	Valles Caldera Mixed Conifer	2013/05	106.53°W, 35.89°N	Evergreen Needleleaf Forests	2007–2021	AmeriFlux
US-SO2	Sky Oaks- Old Stand	2003/07	116.62°W, 33.37°N	Closed Shrublands	1997–2006	AmeriFlux
US-Seg	Sevilleta grassland	2009/08	106.72°W, 34.36°N	Grasslands	2007–2021	AmeriFlux
US-Scs	Southern California Climate Gradient - Coastal Sage	2007/10	117.70°W, 33.73°N	Open Shrublands	2006–2016	AmeriFlux
US-Scg	Southern California Climate Gradient - Grassland	2007/10	117.69°W, 33.74°N	Grasslands	2006–2016	AmeriFlux
US-Me2	Metolius mature ponderosa pine	2020/08	121.56°W, 44.45°N	Evergreen Needleleaf Forests	2002–2022	AmeriFlux

by low-severity fires.

For simplicity, all sites were categorized into two broad plant functional types (PFTs) based on the dominant vegetation affected by wildfire: forest, representing evergreen needleleaf and evergreen broadleaf forests (US-Vcm, US-Me2, AU-Wac, AU-Cpr, AU-Tum), and grass/shrub, representing ecosystems dominated by grasslands, shrublands and understory vegetation (US-Seg, US-Scg, US-Scs, AU-Wrr, US-SO2). The selected sites typically provide 9–21 years of EC data, including 2–19 years of pre-fire records and 2–12 years of post-fire recovery. Additionally, six supplementary U.S. sites with EC observations beginning within five years after fire (but lacking pre-fire coverage) were identified (Table. S1). These were excluded from our main pre/post-fire analysis but may offer insights into early recovery patterns.

For all sites, 30-minute GPP and key meteorological variables, including photosynthetic photon flux density (PPFD), air temperature (Ta), and VPD, were extracted. For Australian sites, we used the Level 6 "GPP_LT" product, accessed via the TERN THREDDS data portal (http s://dap.tern.org.au). GPP_LT was derived using a daytime light-response method , in which ecosystem Re was parameterized with the Lloyd–Taylor model to represent its temperature dependence (Lloyd and Taylor, 1994). The raw 30-minute flux measurements were processed according to OzFlux quality assurance and quality control (QA/QC) protocols and corrected for known biases (Isaac et al., 2017). For U.S. sites in the AmeriFlux network (https://ameriflux.lbl.gov/), we used the GPP_NT_VUT_USTAR50 product, following the FLUXNET standardized pipeline. This product estimated GPP using nighttime partitioning (Reichstein et al., 2005), with Re parameterized from nighttime NEE and Ta. To ensure data reliability, an annually varying friction velocity (u*) threshold was derived via bootstrapping and applied to remove low-turbulence periods known to cause underestimation (Papale et al., 2006). All 30-minute records were screened to remove low-quality or physically implausible GPP values (e.g., negatives). The cleaned data were aggregated to 8-day and monthly intervals to match the temporal resolution of remote sensing products, retaining aggregates only when

more than 60 % of the underlying high-frequency data passed QA filters to ensure consistency and reliability in subsequent analyses.

2.2. Remote sensing proxies

To evaluate post-fire changes in carbon uptake and vegetation condition, we compiled a suite of widely used remote sensing proxies, including five GPP products, one reconstructed SIF dataset, one structural variable (LAI), and one spectral vegetation index (NIRv). All selected products provided continuous temporal coverage across every fire-affected site, spanning both pre- and post-fire periods.

2.2.1. Satellite-based GPP products

The five GPP products used in this study cover the major methodological categories of satellite-based GPP estimation, including process-based models, machine learning approaches, and LUE models, as well as an SIF-based empirical product. These products represented diverse modeling approaches and input sources. BESS v2.0 is a process-based model that integrates canopy radiative transfer, biochemical photosynthesis, and energy balance, driven by MODIS surface parameters and meteorological data, providing daily GPP at 0.05° resolution (Li et al., 2023) (https://www.environment.snu.ac.kr/bessv2). FLUXCOM-X-BASE uses machine learning (XGBoost) to upscale tower GPP based on MODIS vegetation indices and ERA5 climate data, available at 0.25° daily and 0.05° monthly resolution (Nelson et al., 2024) (https://gitlab.gwdg.de/fluxcom/fluxcomxdata). FluxSat v2.2 is a neural network-based GPP product trained on FLUXNET observations using MODIS BRDF-corrected reflectance and incident photosynthetically active radiation (PAR) as inputs, also delivered at 0.05° and daily scale (Joiner et al., 2018) (https://avdc.gsfc.nasa.gov/pub/tmp/FluxSat_GPP/). MODIS GPP (MYD17A2H) is a widely used LUE-based product estimating GPP as a function of APAR, maximum LUE, and meteorological stress scalars, available at 500 m resolution and 8-day composites (Running et al., 2004) (https://ladsweb.modaps.eosdis.nasa.gov/missions-and-measurements/products/MYD17A2H/). GOSIF GPP is derived by applying empirical SIF-GPP regressions to the global GOSIF SIF dataset, producing 0.05° GPP at 8-day intervals (Li and Xiao, 2019b) (https://globalecology.unh.edu/data/GOSIF-GPP.html). For simplicity, we refer to these datasets as BESS GPP, FLUXCOM GPP, FluxSat GPP, GOSIF GPP, and MODIS GPP in subsequent sections. To reduce uncertainties from individual products, we also calculated an ensemble mean GPP (RS GPP$_{Avg}$) across the five datasets.

2.2.2. Other functional and structural proxies

To complement GPP, we included three additional proxies. GOSIF provides 8-day reconstructed SIF estimates at 0.05° resolution using machine learning models trained on OCO-2 data and MODIS reflectance, and MERRA-2 meteorology (Li and Xiao, 2019a) (https://globalecology.unh.edu/data/GOSIF.html). GLASS LAI v6 is a globally consistent LAI dataset generated using a bidirectional long short-term memory (Bi-LSTM) model trained on MODIS reflectance and multiple reference LAI datasets, offering improved seasonal dynamics (Ma and Liang, 2022) (https://glass.bnu.edu.cn/introduction/LAI.html). NIRv was calculated from the MODIS MCD43A4 BRDF-adjusted surface reflectance product (500 m) using the following equation:

$$NIRv = \left(\frac{NIR - RED}{NIR + RED}\right) \times NIR \tag{1}$$

where NIR and RED are reflectance in the near-infrared and red bands, respectively. NIRv is a spectral proxy for photosynthetic capacity and has been shown to correlate well with GPP across biomes (Badgley et al., 2019, 2017).

All remote sensing datasets were resampled to a common 0.05° spatial resolution using bilinear interpolation and aggregated to 8-day and monthly temporal scales for consistency. At each flux tower site,

remote sensing variables were extracted from the 0.05° grid cell containing the tower coordinates. FLUXCOM-X-BASE GPP was used at a spatial resolution of 0.25° with an 8-day temporal resolution, and at 0.05° with a monthly temporal resolution. Dataset specifications were summarized in Table 2. To illustrate the temporal coverage and seasonal dynamics of the remote sensing proxies, Fig. S2 showed representative time series from one forest site (US-Vcm) and one shrub site (US-SO2), alongside EC GPP. The figure demonstrated multi-year consistency and variability across GPP, SIF, LAI, and NIRv before and after fire.

2.3. Evaluation of remote sensing proxy performance in capturing fire-induced vegetation response

To evaluate the performance of remote sensing proxies in capturing vegetation responses to wildfire, we conducted comparative analyses between EC GPP and multiple satellite-derived products across all selected flux tower sites. To explore potential biome-specific differences in disturbance impacts and recovery patterns, sites were grouped into two PFTs—forest and grass/shrub, and all subsequent analyses were conducted and presented separately for these two PFTs.

2.3.1. Proxy–EC GPP relationship analysis

We first assessed the relationship between each satellite-based proxy and EC GPP before and after fire disturbance. For each site, equal-length pre- and post-fire periods were defined, with the post-fire window starting from the first available EC GPP record following the fire event. Linear regression was applied to both pre- and post-fire periods separately using all eight remote sensing variables: five GPP products (BESS GPP, FLUXCOM GPP, FluxSat GPP, GOSIF GPP, MODIS GPP), GOSIF SIF, GLASS LAI, and NIRv. Regression slope and coefficient of determination (R^2) were used to evaluate the temporal consistency and disturbance sensitivity of each proxy. This analysis revealed how well each satellite proxy reproduced the carbon fluxes observed by EC towers, and whether this relationship shifted under fire disturbance. To statistically evaluate fire-induced alterations in the relationship between satellite proxies and EC GPP, we conducted independent samples t-tests to compare regression slopes from pre- and post-fire periods. Statistical significance was assessed at three levels: ***$p < 0.001$, **$p < 0.01$, and *$p < 0.05$.

2.3.2. Fire-induced loss and change metrics

To quantify the magnitude of fire-induced loss and functional/structure shifts, we calculated two complementary indicators for each remote sensing proxy. The maximum relative decrease (MRD) characterizes the most severe immediate decline following fire, defined as the relative difference between the pre-fire mean and the post-fire minimum value:

Table 2

Overview of remote sensing datasets used in this study. Listed products include gross primary production (GPP), leaf area index (LAI), solar-induced chlorophyll fluorescence (SIF), and near-infrared reflectance of vegetation (NIRv). Spatial and temporal resolutions correspond to the native format of each dataset.

Product	Variable	Spatial resolution	Temporal resolution	Data coverage
BESS (v2.0)	GPP	0.05°	daily, monthly	1982–2022
FLUXCOM (FLUXCOM-X-BASE)	GPP	0.25°, daily (0.05°, monthly)	daily, monthly	2001–2021
FluxSat (v2.2)	GPP	0.05°	daily	2000–2024
GOSIF	GPP	0.05°	8 d, monthly	2000–2024
MODIS (MYD17A2H)	GPP	500 m	8 d	2002—present
GLASS (v60)	LAI	0.05°	8 d	2000–2024
GOSIF	SIF	0.05°	8 d, monthly	2000–2024
MODIS (MCD43A4)	NIRv	500 m	daily	2000–present

$$MRD = \frac{X_{pre-fire\ mean} - X_{post-fire\ min}}{X_{pre-fire\ mean}} \qquad (2)$$

where X denotes the value of a given proxy such as GPP, SIF, LAI, or NIRv. To assess longer-term changes, we computed the mean relative change (MRC), calculated as the relative difference between post-fire and pre-fire mean values:

$$MRC = \frac{\left|X_{post-fire\ mean} - X_{pre-fire\ mean}\right|}{X_{pre-fire\ mean}} \qquad (3)$$

MRD highlights the acute severity of fire-induced degradation, while MRC captures the persistent shifts in vegetation functional/structural state. Together, they offer a dual perspective on proxy sensitivity to fire disturbances. For consistency, the pre- and post-fire periods used in MRD and MRC calculations were identical to those applied in the proxy—EC GPP relationship analysis.

2.3.3. Post-fire carbon gain estimation

To assess ecosystem productivity recovery, we calculated accumulated GPP for each site and GPP product, from the first available EC GPP record post-fire through the end of the analysis period. This metric reflected the total post-disturbance carbon uptake and enabled direct comparison between ground-based and remote estimates of carbon gain. Only GPP products were included due to the requirement for absolute flux quantification. Accumulated GPP integrated temporal recovery and provided insights into potential under- or over-estimation of post-fire productivity by remote sensing proxies.

2.3.4. Vegetation recovery trajectory metrics

To characterize post-fire vegetation recovery dynamics, we calculated two commonly used metrics: time to recovery (TTR) and GPP recovery rate (RecR). TTR was defined as the number of days between the post-fire minimum and the point at which the proxy value returned to 80 % of its pre-fire mean, a threshold chosen to ensure consistent recovery estimates across sites and products where full recovery was often not reached. We also evaluated a 50 % threshold to assess the robustness of our recovery metrics. Based on TTR, the RecR was computed as the slope of the recovery trajectory, representing the speed of return toward pre-disturbance conditions. It was calculated as:

$$RecR = \frac{X_{pre-fire\ A\%} - X_{post-fire\ min}}{TTR} \qquad (4)$$

where $X_{pre-fire\ A\%}$ is 50 % or 80 % of the pre-fire mean. RecR was computed only for GPP products due to its dependence on absolute carbon uptake values. Prior to metric calculation, all-time series were smoothed using a three-point moving average and then detrended and deseasonalized to isolate fire-induced signals (Fig. 2). These trajectory-

based indicators complemented magnitude-based metrics (MRD, MRC, accumulated GPP) by explicitly capturing the timing and pace of ecosystem functional return.

To further evaluate the consistency between remote sensing proxies and EC GPP in depicting TTR and RecR, we employed Taylor diagrams. These diagrams provided a concise statistical summary by simultaneously representing the correlation coefficient (r), the standard deviation (SD), and the centered root mean square difference (CRMSD) between each remote sensing proxy and EC GPP. This approach allowed for a comprehensive comparison of the performance of different proxies in capturing the magnitude and temporal patterns of ecosystem recovery.

2.3.5. Climate sensitivity analysis

To assess whether fire altered GPP—climate coupling, and whether such shifts were detectable by remote sensing proxies, we selected two representative sites—one forest and one grass/shrub—with the most complete GPP and meteorological data before and after fire. For each GPP product and GOSIF, we applied linear regressions relating their values to three key drivers: PPFD, Ta, and VPD, separately for the pre- and post-fire periods. By applying independent samples t-tests to assess the significance of pre- versus post-fire regression slope differences (***$p < 0.001$, **$p < 0.01$, *$p < 0.05$), in conjunction with comparisons of R^2 values, we systematically evaluated the whether proxies consistently captured shifts in climate sensitivity under fire-modified conditions.

All data preprocessing and statistical analyses were performed in Python (v3.9). Results reported in the main text were based on 8-day resolution data, while complementary monthly-scale results were presented in the Supplementary Materials.

3. Result

3.1. Shifts in proxy–EC GPP relationships before and after fire in forest

The relationships between remote sensing proxies and EC GPP exhibited pronounced shifts following fire disturbances at forest sites. Across all satellite proxies, regression slopes increased markedly after fire (Fig. 3 and Fig. 5a). Among satellite GPP products, FLUXCOM GPP, FluxSat GPP, and GOSIF GPP showed substantially underestimated pre-fire slopes (0.69, 0.57, and 0.66), which rose to near or above 1 post-fire (1.00, 0.91, and 1.07), indicating reduced underestimation after fire. In contrast, BESS GPP and MODIS GPP had pre-fire slopes already close to 1 (0.98 and 0.93), but increased disproportionately after fire, reaching 1.53 and 1.45, suggesting post-fire overcompensation. RS GPP$_{Avg}$ followed a similar trend, increasing from 0.77 to 1.19. Notably, the post-fire scatter points for most GPP products were distributed above the 1:1 line, indicating a tendency to overestimate GPP relative to EC GPP under post-disturbance conditions. Vegetation indices also showed
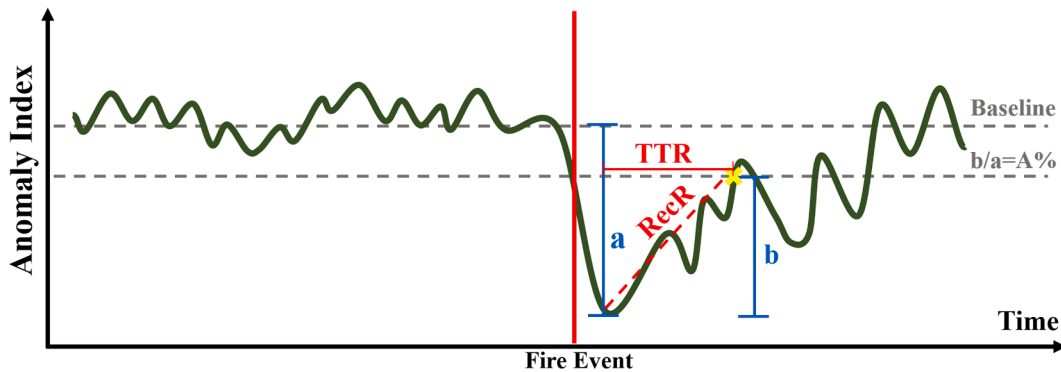

Fig. 2. Conceptual diagram of post-fire vegetation recovery indicators. The Anomaly Index represents the smoothed and detrended time series of vegetation proxies. The red vertical line marks the timing of the wildfire. TTR indicates the duration from the post-fire minimum to the point when the variable reaches 50 % or 80 % of its pre-fire baseline. RecR represents the slope of this recovery trajectory and quantifies how quickly the ecosystem returns toward its pre-fire condition.
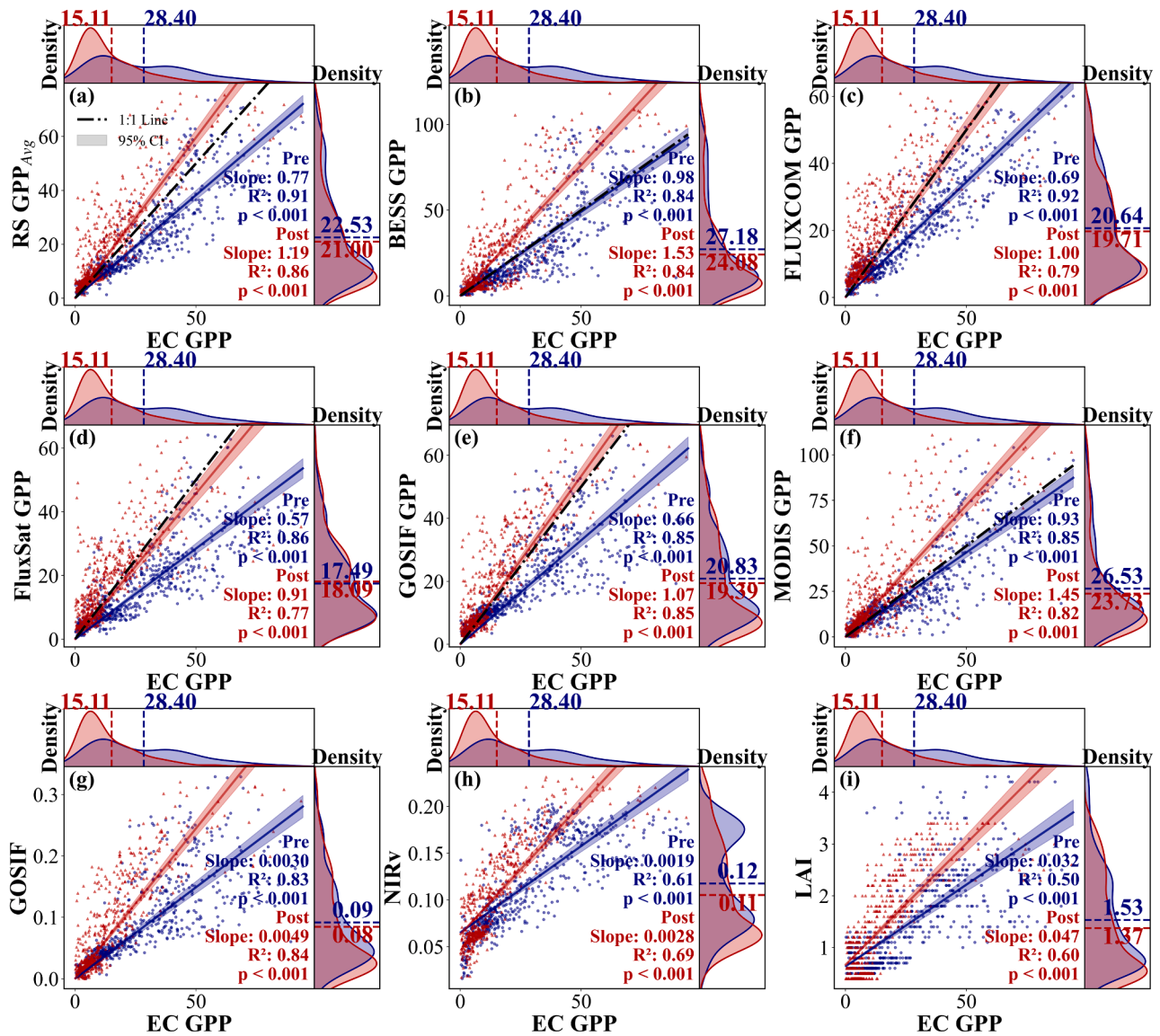
Fig. 3. The relationship between 8-day EC GPP and various remote sensing proxies at forest sites, separated by pre-fire (blue) and post-fire (red) periods. Each panel compares EC GPP with RS GPP$_{Avg}$ (a), BESS GPP (b), FLUXCOM GPP (c), FluxSat GPP (d), GOSIF GPP (e), MODIS GPP (f), GOSIF (g), NIRv (h), and LAI (i). Solid lines represent linear regression fits for pre- and post-fire periods, and dashed lines indicate the 1:1 line for reference (a–f). Regression slopes and coefficients of determination (R^2) for pre- and post-fire periods are shown in each panel. Marginal density plots show distributions of pre- and post-fire values along both axes. Numerical annotations indicate the mean EC GPP and proxy values before and after fire. Units: GPP (g C m^{-2} 8 d^{-1}), GOSIF (W m^{-2} μm^{-1} sr^{-1}), LAI (m^2 m^{-2}).

enhanced coupling with EC GPP after fire. The slope of GOSIF increased from 0.0030 to 0.0049, NIRv from 0.0019 to 0.0028, and LAI from 0.032 to 0.047, indicating stronger post-fire correspondence with flux observations despite lower absolute magnitude. In terms of model performance, R^2 declined for most satellite GPP products after fire, e.g., FLUXCOM GPP from 0.92 to 0.79 and FluxSat GPP from 0.86 to 0.77 (Fig. 5b), reflecting weakened agreement with EC GPP under disturbance. Conversely, LAI and NIRv exhibited slight R^2 improvements, from 0.50 to 0.60 and 0.61 to 0.69, respectively, though they remained less predictive overall. The mean EC GPP at forest sites decreased from 28.40 to 15.11 g C m^{-2} 8 d^{-1} after fire, while satellite proxies showed smaller reductions, e.g., MODIS GPP from 26.53 to 23.73 g C m^{-2} 8 d^{-1}, and BESS GPP from 27.18 to 24.08 g C m^{-2} 8 d^{-1}.

In contrast, grass and shrub sites showed relatively stable proxy–GPP relationships across fire disturbance (Fig. 4 and Fig. 5c–d). Most GPP products exhibited minimal changes in slope, e.g., RS GPP$_{Avg}$ changed slightly from 0.73 pre-fire to 0.72 after fire. Regression lines consistently fell below the 1:1 line, reflecting continued underestimation before and

after fire. Post-fire R^2 values declined slightly across all proxies. The mean EC GPP declined modestly from 26.44 to 21.73 g C m^{-2} 8 d^{-1}, and satellite proxies exhibited similar reductions (e.g., BESS GPP: from 22.63 to 16.69 g C m^{-2} 8 d^{-1}; MODIS GPP: from 26.67 to 20.78 g C m^{-2} 8 d^{-1}), suggesting better agreement between proxy and observation in capturing fire-driven declines in grass/shrub ecosystems. These patterns of slope and R^2 changes were consistent when using monthly-aggregated data (Fig. S3–S5), confirming the robustness of fire-induced shifts in proxy–GPP relationships across temporal resolutions.

3.2. Underestimation of fire-induced loss by remote sensing proxies

Remote sensing proxies systematically underestimated fire-induced reductions in vegetation loss relative to EC GPP (Fig. 6a–d), particularly at forest sites. At forest sites, EC GPP exhibited the MRD of 94.3 %, whereas MODIS GPP (87.0 %) and BESS GPP (75.4 %) provided the closest estimates among satellite GPP products. FLUXCOM GPP (61.4 %), and FluxSat GPP (58.5 %) showed more substantial
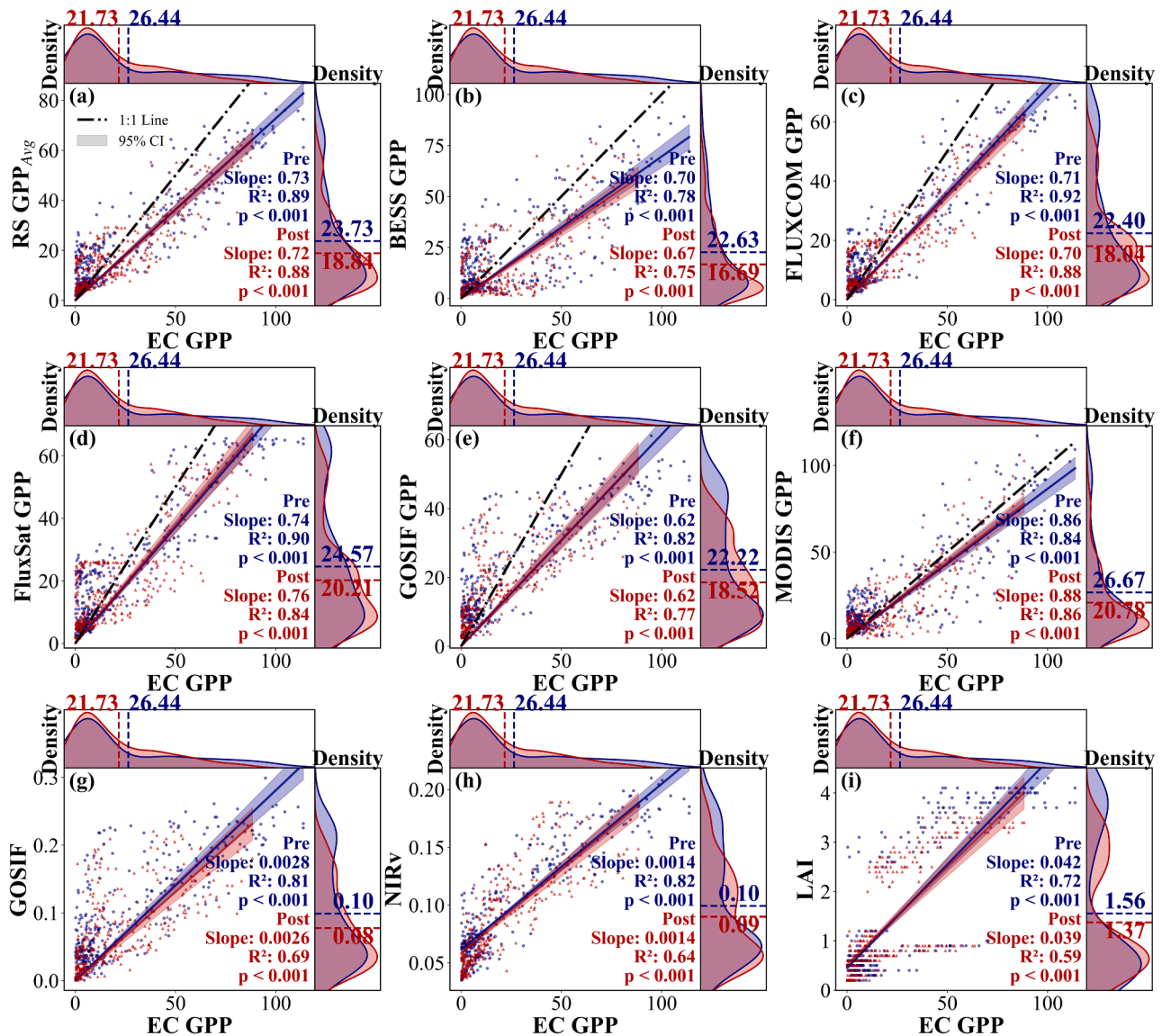
Fig. 4. The relationship between 8-day EC GPP and various remote sensing proxies at grass/shrub sites, separated by pre-fire (blue) and post-fire (red) periods. Each panel compares EC GPP with RS GPP_{Avg} (a), BESS GPP (b), FLUXCOM GPP (c), FluxSat GPP (d), GOSIF GPP (e), MODIS GPP (f), GOSIF (g), NIRv (h), and LAI (i). Solid lines represent linear regression fits for pre- and post-fire periods, and dashed lines indicate the 1:1 line for reference (a–f). Regression slopes and coefficients of determination (R^2) for pre- and post-fire periods are shown in each panel. Marginal density plots show distributions of pre- and post-fire values along both axes. Numerical annotations indicate the mean EC GPP and proxy values before and after fire. Units: GPP (g C m^{-2} 8 D^{-1}), GOSIF (W m^{-2} μm^{-1} sr^{-1}), LAI (m^2 m^{-2}).

underestimation, while the ensemble RS GPP_{Avg} and GOSIF GPP recorded 68.4 % and 67.2 %, respectively. GOSIF, while not a GPP product, yielded an MRD of 80.3 %, performing between the higher-sensitivity MODIS/BESS GPP and the lower-sensitivity FLUXCOM/FluxSat GPP. By contrast, NIRv (53.7 %) and LAI (47.3 %) captured only minor declines, indicating limited sensitivity to fire-induced functional loss. At grass/shrub sites, EC GPP declined by 83.4 %, while MODIS GPP, BESS GPP, GOSIF GPP and GOSIF recorded MRDs of 85.0 %, 84.9 %, 79.9 %, and 89.2 %, respectively. Other proxies, including FLUXCOM GPP, FluxSat GPP, and NIRv ranged from 50 % to 62 %, while LAI remained the lowest (28.1 %). Overall, MODIS GPP, BESS GPP and GOSIF provided the closest MRD estimates to EC GPP across sites.

The MRC results demonstrated even larger gaps between remote sensing proxies and EC GPP. At forest sites, EC GPP declined by 52.8 %, while satellite GPP products showed notably smaller changes: MODIS GPP (19.2 %), BESS GPP (32.7 %), FLUXCOM GPP (16.6 %), FluxSat GPP (15.7 %), GOSIF GPP (15.3 %), and RS GPP_{Avg} (19.8 %). NIRv, LAI and GOSIF were 16.1 %, 19.1 %, and 18.7 %, respectively. At grass and

shrub sites, MRC was overall lower compared to forest sites. EC GPP declined by 34.3 %, while BESS GPP (23.5 %), and GOSIF (21.2 %) again showed relatively close alignment. Other proxies ranged from 10 % to 18 %. Similar trends in MRD and MRC were observed when using monthly data (Fig. S6), suggesting that the underestimation was not substantially influenced by temporal resolution.

3.3. Overestimation of post-fire carbon gain in forests

Satellite GPP products generally overestimated post-fire carbon gain relative to EC GPP, particularly at forest sites (Fig. 7a–e, Fig. 8a–b). Across the five forest sites, cumulative EC GPP exhibited slower and more gradual recovery trajectories, whereas BESS GPP and MODIS GPP often estimated −650–2100 g C m^{-2} higher cumulative carbon uptake over the post-fire period. For example, within five years post-fire, MODIS GPP exceeded EC GPP by 23 % at US-Vcm and 46 % at AU-Wac, whereas BESS GPP overestimated EC GPP by 61 % and 44 % at the same sites. FLUXCOM GPP, FluxSat GPP and GOSIF GPP also showed
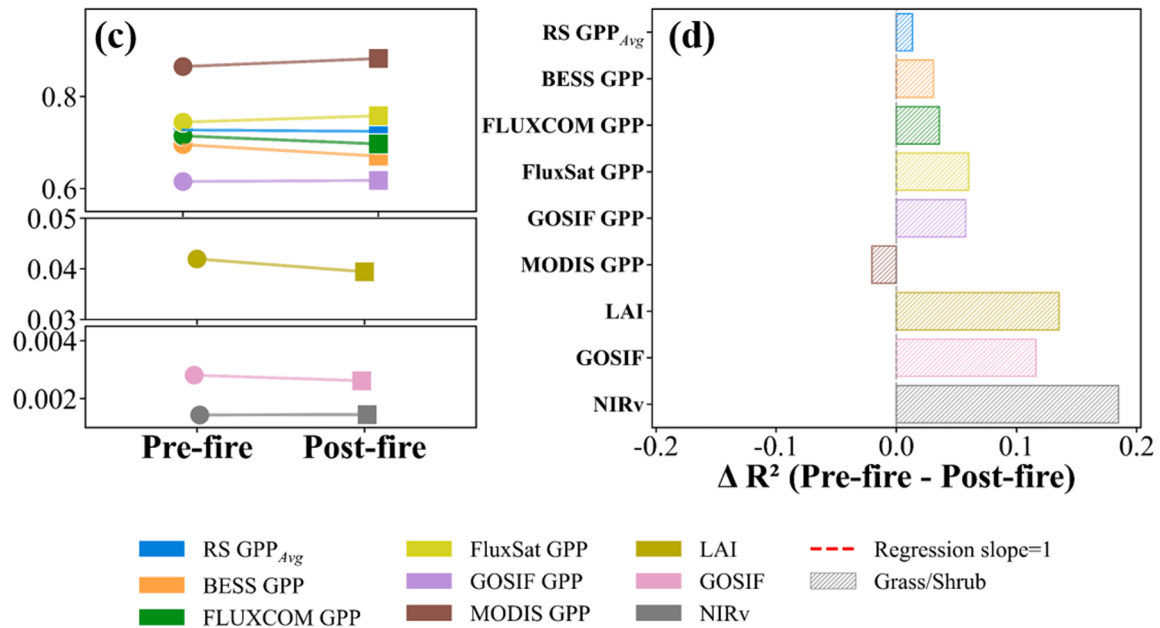
Forest
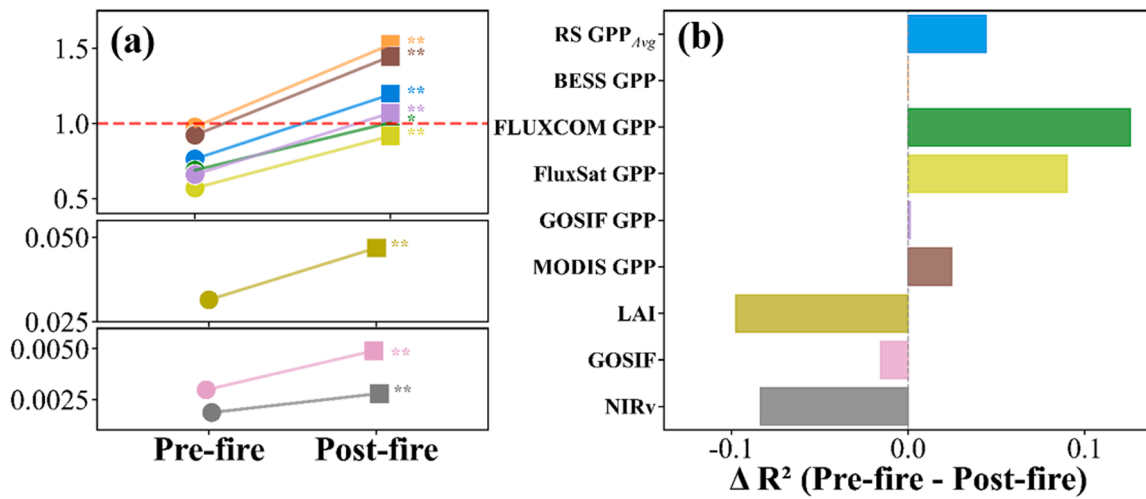
Grass/Shrub

Fig. 5. Summary of regression slopes and changes in R^2 between 8-day EC GPP and remote sensing proxies before and after fire. (a-b) correspond to forest sites, showing pre- and post-fire regression slopes and ΔR^2 (pre-fire minus post-fire), respectively. (c-d) show corresponding results for grass/shrub sites. Colored markers represent different proxies. The red dashed line in (a) indicates a slope of 1.0, aiding comparison with ideal agreement. Asterisks indicate statistical significance levels for pre- vs. post-fire differences (*$p < 0.05$, **$p < 0.01$, ***$p < 0.001$).

overestimations, albeit to a lesser extent (-500 to 1400 g C m^{-2} across the five sites within the post-fire period). An exception was the AU-Cpr site, where all remote sensing GPP products were largely consistent with EC GPP and showed no systematic overestimation. Sites with observations limited to the post-fire period likewise exhibited a comparable overestimation pattern (Fig. S7). First-year post-fire comparisons (Fig. 8a–b) further underscore this discrepancy: the mean cumulative EC GPP in forest sites during the first post-fire year was 338 g C m^{-2} yr^{-1}, whereas MODIS and BESS GPP averaged over 710 g C m^{-2} yr^{-1}. Other satellite GPP products showed smaller differences relative to EC GPP (ranging from 240 to 320 g C m^{-2} yr^{-1}) but still exhibited a tendency toward overestimation. Additionally, the absolute difference between EC GPP and remote sensing products increased progressively with time since the fire, especially at forest sites with longer recovery periods. This

pattern was observed in both full-cycle and post-fire-only sites (Fig. S8a–d, S9a–c). For example, at the US-Vcm site, the difference in RS GPP$_{Avg}$ increased from 199 g C m^{-2} in the first-year post-fire to 1322 g C m^{-2} by the eighth-year post-fire.

At grass and shrub sites, post-fire remote sensing GPP was generally more consistent with EC GPP, though modest overestimation remained at some sites (Fig. 7f–j, Fig. 8c–d). For example, at the US-Seg and US-Scs sites, multi-year cumulative differences between EC GPP and most remote sensing products remained within ±30 %, indicating relatively good agreement. In contrast, at the US-Scg and AU-Wrr sites, substantial discrepancies were observed among products, with the difference between MODIS GPP and EC GPP reaching 2427 g C m^{-2} yr^{-1} and 902 g C m^{-2} yr^{-1}, respectively. First-year post-fire cumulative EC GPP at grass and shrub sites ranged widely from 213 g C m^{-2} yr^{-1} at US-Seg to 1955 g C m^{-2}
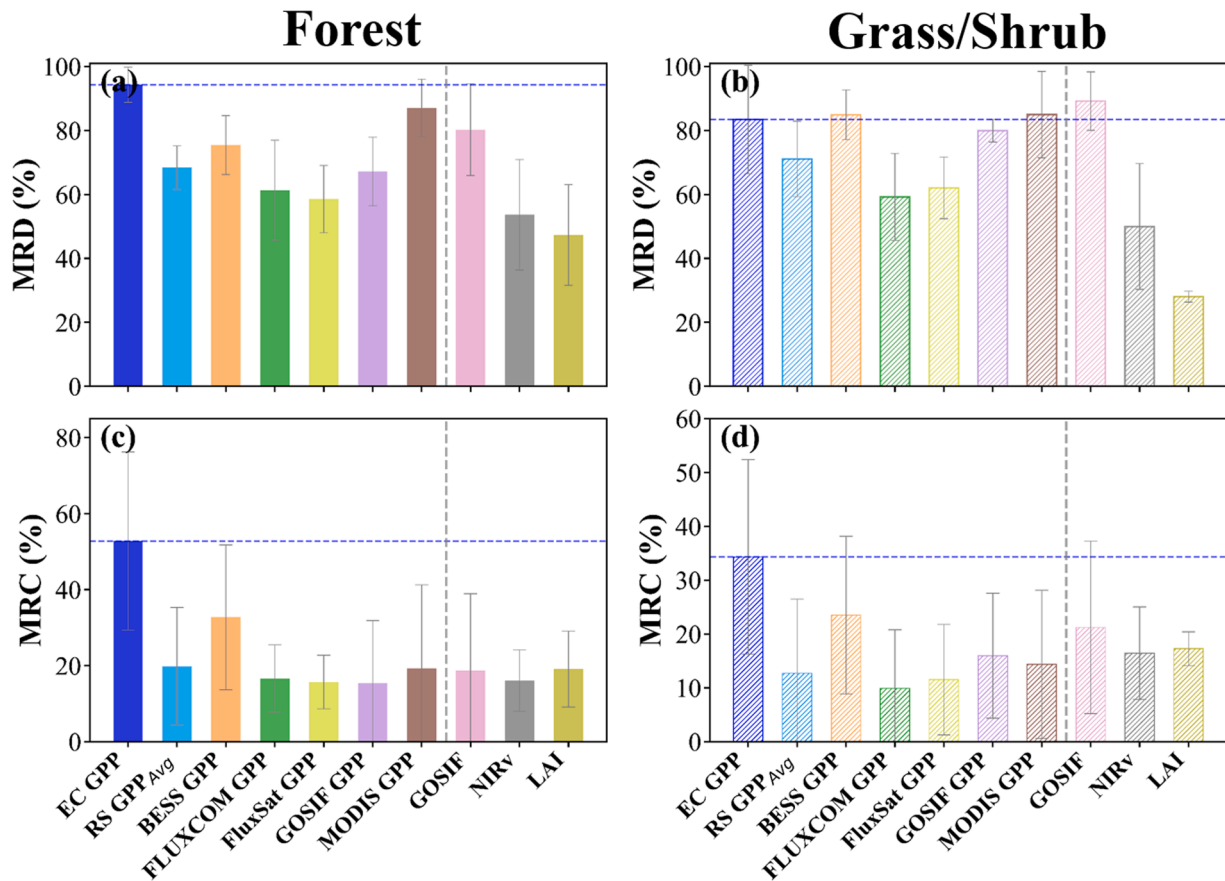
Fig. 6. Post-fire reductions in 8-day EC GPP and remote sensing proxies. Maximum relative decrease (MRD, %) in EC GPP and remote sensing proxies at forest (a) and grass/shrub (b) sites. Mean relative change (MRC, %) before and after fire for the same set of variables at forest (c) and grass/shrub sites (d). Error bars indicate inter-site variability. Blue dashed lines mark the EC GPP mean as a reference.

yr^{-1} at AU-Wrr. Similar to forests, differences between remote sensing GPP and EC GPP increased with time (Fig. S8e–i, Fig. S9d–e). When averaged across all grass/shrub sites, however, the cumulative post-fire GPP from remote sensing products remained relatively close to EC GPP, indicating better overall agreement than in forest ecosystems (Fig. 8d).

Overall, these findings indicated that satellite GPP products-especially MODIS and BESS, tended to overestimate post-fire carbon gain in forest ecosystems. This overestimation became more pronounced over longer time spans and was less evident in grass and shrub systems.

3.4. Differences in post-fire recovery time and rate among proxies

We further examined post-fire vegetation recovery dynamics using two quantitative metrics—TTR and RecR—across forest and grass/shrub sites (Fig. 9). Only proxies whose TTR fell entirely within the study period were included.

At forest sites, EC GPP showed a mean TTR of ~350 days (Fig. 9a). BESS GPP, GOSIF GPP, and GOSIF produced relatively close estimates (270–360 days), whereas FLUXCOM GPP, FluxSat GPP, MODIS GPP, RS GPP$_{Avg}$ and NIRv reported notably shorter recovery times (60–200 days), suggesting an earlier recovery signal in satellite products. At grass/shrub sites (Fig. 9b), TTRs were much lower for all proxies, with EC GPP averaging ~50 days. Most GPP products (BESS GPP, FLUXCOM GPP, FluxSat GPP, GOSIF GPP, MODIS GPP, RS GPP$_{Avg}$) fell within 45–75 days, while LAI had a slightly higher mean TTR (~105 days) and large variability. LAI recovery was not estimated for forest sites due to incomplete recovery within the observation period.

For RecR, EC GPP showed higher post-fire growth rates at both forest and grass/shrub sites compared to most satellite proxies (Fig. 9c–d). At

forest sites, the RecR of EC GPP averaged 0.018 g C m^{-2} D^{-2}. BESS GPP exhibited a comparable recovery rate (0.018 g C m^{-2} D^{-2}), while MODIS GPP showed a slightly higher rate (0.029 g C m^{-2} D^{-2}). In contrast, FLUXCOM GPP, FluxSat GPP, RS GPP$_{Avg}$ and GOSIF GPP displayed lower recovery rates (0.008–0.013 g C $m^{-2}$$_{D}^{-2}$), indicating a slower recovery pace (Fig. 9c). At grass/shrub sites, EC GPP exhibited a mean RecR of 0.038 g C $m^{-2}$$_{D}^{-2}$, higher than most satellite proxies except for MODIS GPP (0.032 g C m^{-2} D^{-2}) and BESS GPP (0.036 g C m^{-2} D^{-2}), which showed good agreement (Fig. 9d). GOSIF GPP, FluxSat GPP, FLUXCOM GPP and RS GPP$_{Avg}$ tended to underestimate recovery rates across both ecosystems. Additionally, we found that these observed patterns and conclusions were consistent and robust across both the 50 % and 80 % recovery thresholds (Fig. S10).

To further evaluate the consistency of remote sensing proxies in capturing vegetation recovery dynamics across sites, we compared TTR and RecR performance using Taylor diagrams based on the 80 % recovery threshold (Fig. 10). For TTR, BESS GPP, GOSIF GPP, and GOSIF demonstrated the highest agreement with EC GPP, showing SD ratio to 1 and high correlation coefficients ($r > 0.95$), along with low CRMSE values (CRMSE < 1). Other proxies, such as FLUXCOM GPP, RS GPP$_{Avg}$, MODIS GPP and NIRv, exhibited high correlations but underestimated variability, resulting in SD ratios that deviated further from 1 (SD ratio < 0.5) (Fig. 10a). For RecR, MODIS GPP and BESS GPP showed stronger correspondence with EC GPP in both correlation ($r > 0.6$) and variability. In contrast, FluxSat GPP, GOSIF GPP, RS GPP$_{Avg}$ and FLUXCOM GPP presented larger deviations (SD ratio < 0.5), indicating underestimation of recovery rates or inconsistent patterns (Fig. 10b). The Taylor diagram results support earlier findings from Fig. 9, reaffirming that BESS GPP, GOSIF GPP, and GOSIF provided the most consistent
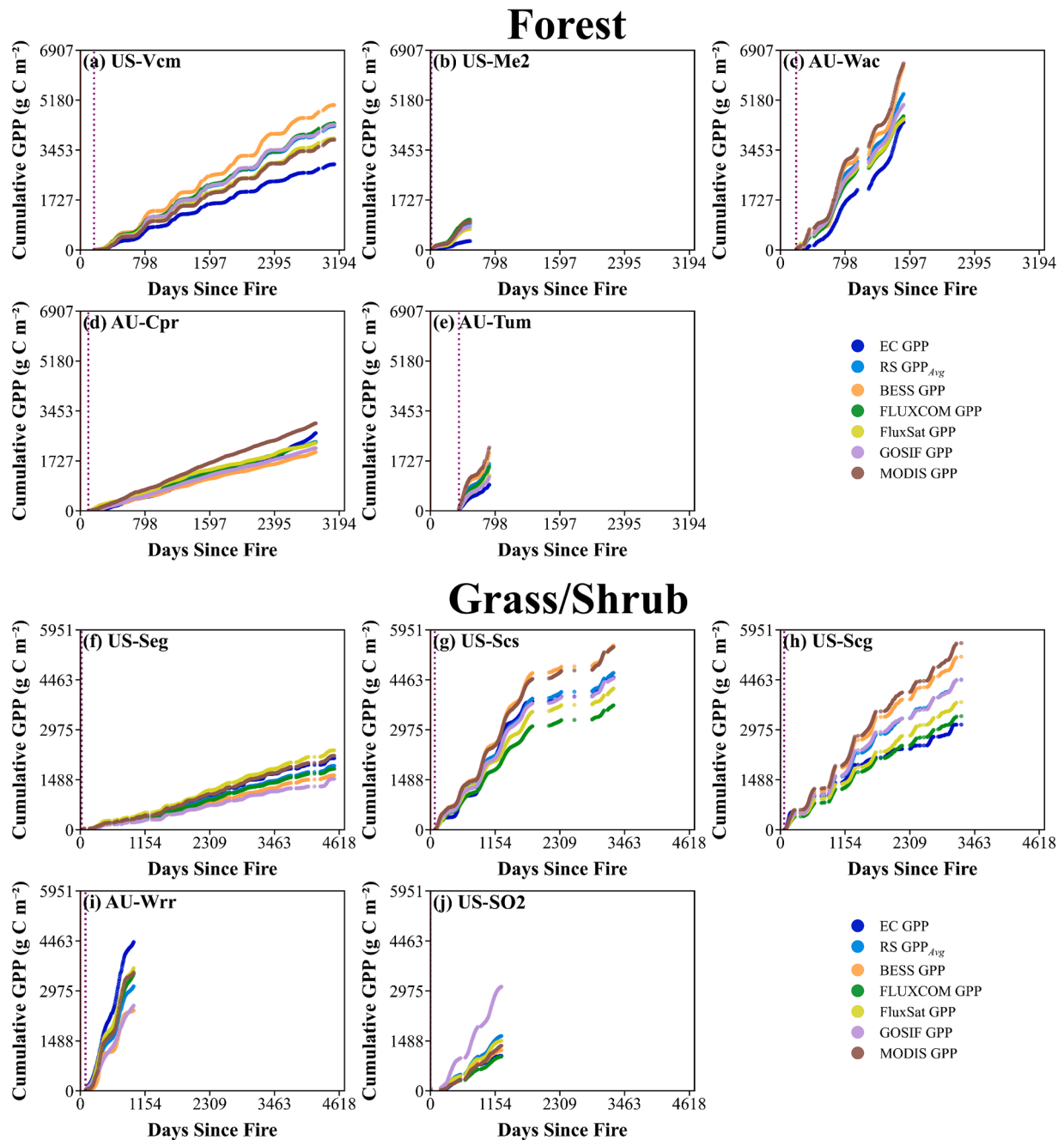
Fig. 7. Cumulative GPP following fire across flux tower sites. (a–e) show forest sites, and (f–j) show grass and shrub sites. The purple dashed line marks the start of the post-fire observation window for all products.

estimates of recovery timing, while MODIS GPP and BESS GPP showed better agreement in terms of recovery rates.

3.5. Fire-induced shifts in GPP–climate coupling not captured by satellite GPP

To evaluate whether remote sensing proxies reflect post-fire shifts in GPP–climate coupling, we compared their sensitivities to key meteorological drivers before and after fire at one representative forest site (US-Vcm) (Fig. 11, Fig. S11) and one shrub site (US-SO2) (Fig. S12–13). At the forest site, EC GPP exhibited marked declines in sensitivity (i.e., regression slope) to all three variables–PPFD, Ta, and VPD–after fire disturbance. Specifically, the mean regression slope of EC GPP to PPFD decreased from 0.088 to 0.054, to Ta from 1.60 to 0.94, and to VPD from

3.32 to 1.17. By contrast, satellite GPP products largely failed to capture such declines. Most proxies exhibited stable or even slightly increased sensitivity to PPFD and Ta after fire (Fig. 11a–b), and only moderate reductions in VPD sensitivity (Fig. 11c). For instance, BESS GPP showed minimal or positive shifts in their coupling to light and temperature, diverging from EC GPP patterns. Similarly, MODIS GPP, GOSIF GPP, and FluxSat GPP retained stronger VPD coupling than EC GPP post-fire. GOSIF remained nearly unchanged in its sensitivity to all variables. EC GPP consistently exhibited lower R^2 (Fig. 11d–F) and flatter regression slopes after fire, whereas most remote sensing products also showed reduced R^2 but maintained stable or only slightly altered relationships, particularly in response to Ta and PPFD. This indicates that satellite-based proxies may not adequately capture the physiological response changes of ecosystems or shifts in their climate sensitivity following fire
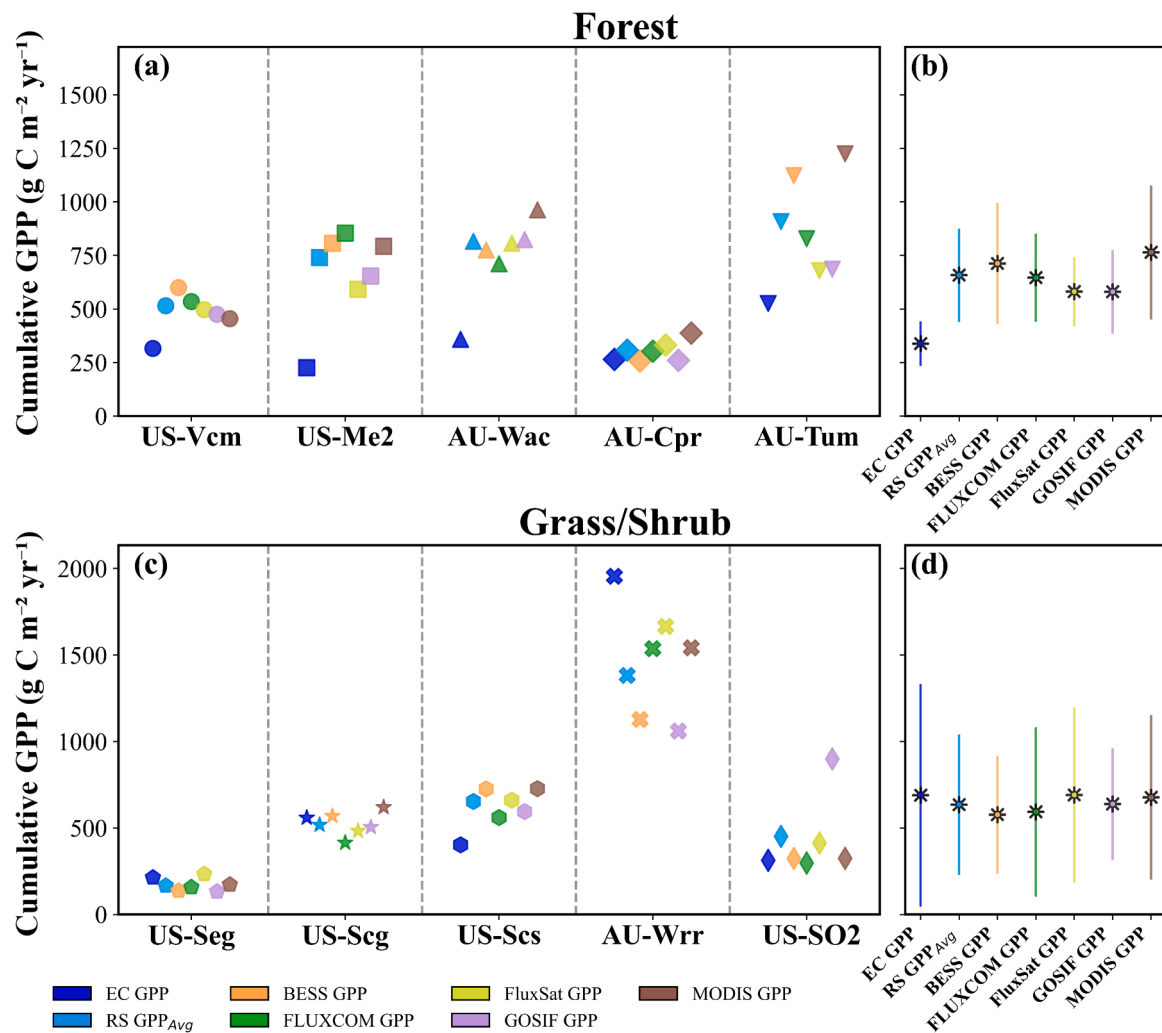
Fig. 8. Comparison of cumulative GPP during the first post-fire year. (a–c) compare cumulative GPP among sites for forest (a) and grass/shrub (c), while (b–d) compare the performance of different products during the first post-fire year for forest (b) and grass/shrub (d).

disturbances.

In contrast to the forest site, the shrub site (US-SO2) demonstrated only minor changes in sensitivity to key meteorological variables before and after fire (Fig. S12–13). The regression slope of EC GPP in response to PPFD increased slightly from 0.015 to 0.026, for Ta from 0.25 to 0.19, and for VPD from 1.64 to 1.06. Remote sensing proxies exhibited similar patterns, with no statistically significant changes in regression slopes to PPFD, Ta, or VPD after fire. The consistency of these sensitivity patterns implies that, within shrub ecosystems, remote sensing indices effectively capture the coupling between carbon fluxes and meteorological variables. This finding contrasts markedly with the forest ecosystem, where sensitivity decreased substantially and satellite products demonstrated inconsistent trend, underscoring ecosystem-specific variability in responses to fire disturbance.

4. Discussion

Wildfires alter carbon dynamics through rapid carbon loss and long-term recovery processes. By comparing remote sensing proxies with EC GPP across burned sites, we found that satellite products generally captured the direction of fire impacts but differed in magnitude and recovery metrics. Remote sensing proxies (satellite GPP, SIF, LAI, NIRv) tended to underestimate carbon loss and overestimate post-fire recovery, with limited sensitivity to changes in climate coupling after fire. These findings highlight key limitations and methodological challenges

in current satellite-based assessments. In the following sections, we synthesize our findings from three perspectives: the performance of remote sensing proxies across different fire stages, contrasts between forest and grass/shrub ecosystems, and key methodological uncertainties and implications for post-fire carbon monitoring.

4.1. Performance of remote sensing proxies in tracking fire-induced GPP dynamics

Our evaluation revealed that different remote sensing proxies varied substantially in their ability to capture fire-induced loss, post-fire recovery, and cumulative carbon gain. While all products broadly reproduced the direction of change, their accuracy diverged across disturbance stages. For fire-induced GPP loss, some satellite GPP products successfully captured the immediate impact but underestimated persistent suppression. MODIS GPP (LUE-based), BESS GPP (process-based) and GOSIF provided the closest estimates of the immediate maximum loss indicated by MRD (Fig. 6a–b). Their relative advantages lie in incorporating physical or semi-empirical representations of photosynthesis, which more directly reflect canopy function and its decline after fire (Running et al., 2004; Ryu et al., 2011). GOSIF—a direct physiological signal of photosynthesis—was more sensitive to functional suppression (Li and Xiao, 2019a). In contrast, machine learning models (FLUXCOM, FluxSat), largely trained on undisturbed ecosystems (Jung et al., 2020; Schimel et al., 2015; Tramontana et al.,
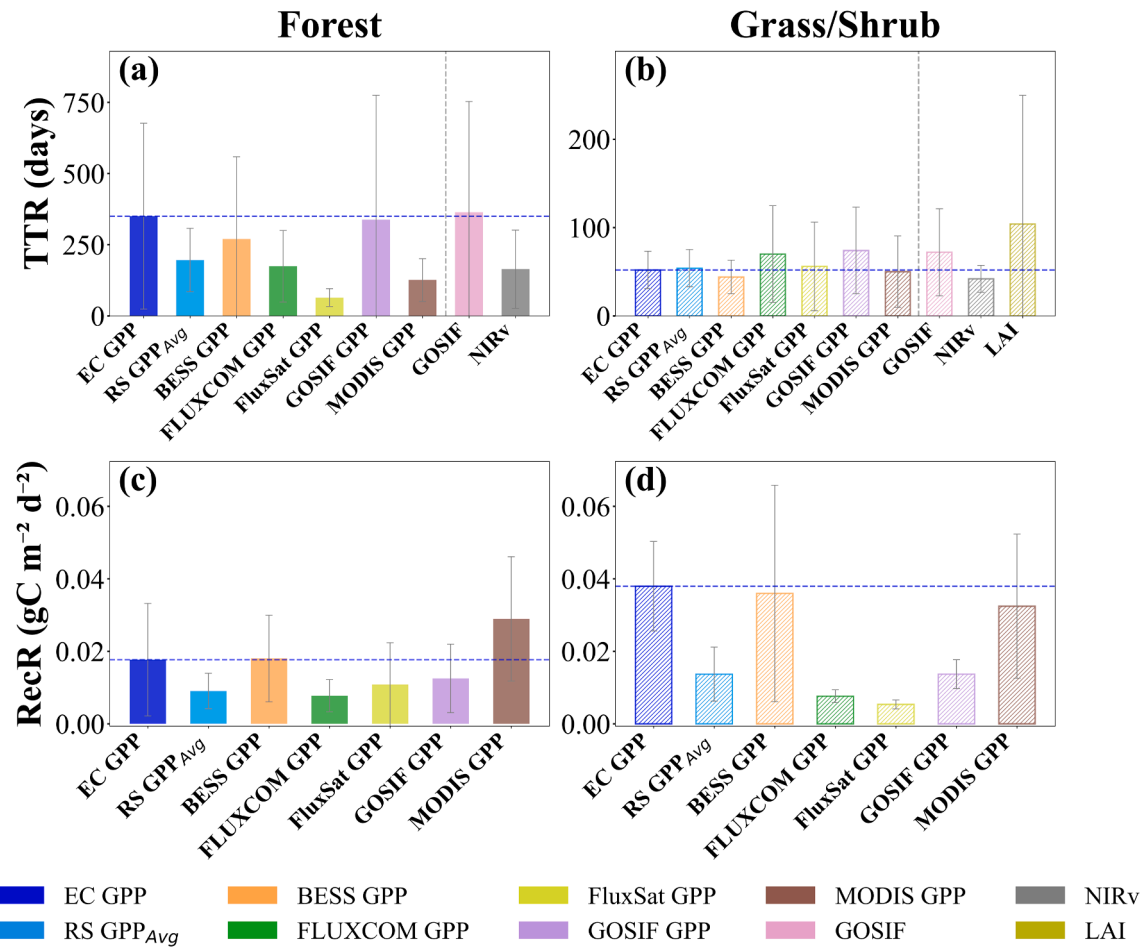
Fig. 9. Vegetation recovery metrics with 80 % recovery threshold. (a) and (b) show the TTR; (c) and (d) show the RecR. (a) and (c) correspond to forest sites, (b) and (d) correspond to grass and shrub sites. The blue dashed lines indicate the mean value of EC GPP, serving as a reference for comparison.
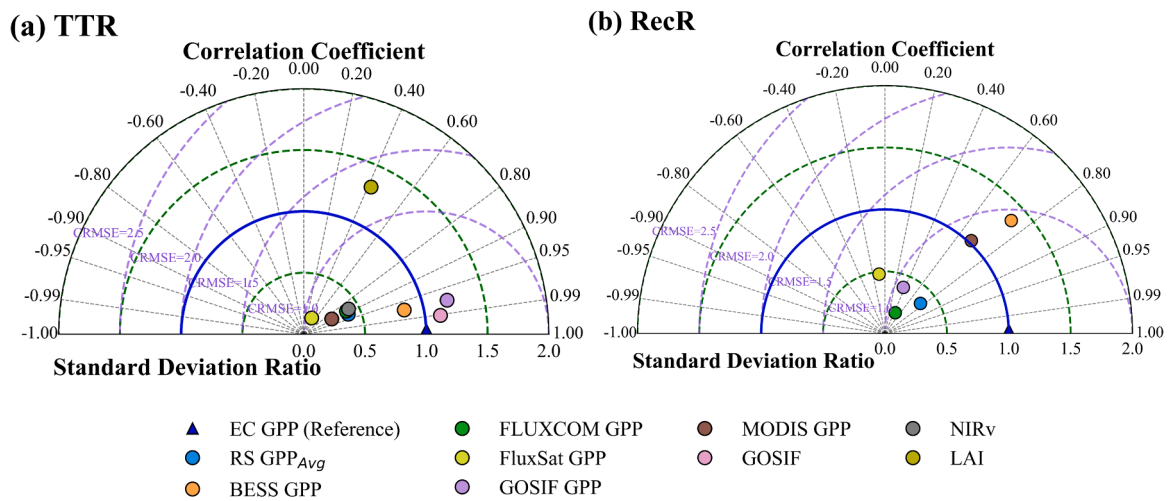

Fig. 10. Taylor diagrams comparing remote sensing proxies against EC GPP for recovery metrics. TTR (a) and RecR (b) are evaluated across all sites. Standard deviation ratio, correlation coefficient, and Centered Root Mean Square Error (CRMSE) contours (purple dashed lines) jointly assess consistency with EC GPP (blue triangles). Proxies closer to the EC reference exhibit better agreement.

2016), underestimated MRD due to limited representation of disturbance-driven processes. However, when considering the persistent change indicated by MRC across recovery periods, all remote sensing products underestimated long-term GPP reduction compared with EC towers (Fig. 6c–d). This mismatch indicates that while some proxies

detect acute canopy loss, they tend to portray ecosystems as recovering too quickly, failing to capture persistent post-fire suppression.

These systematic biases became more evident when examining recovery-related metrics. EC GPP indicated longer TTR in forests, often exceeding one year. While BESS GPP, GOSIF GPP, and GOSIF provided
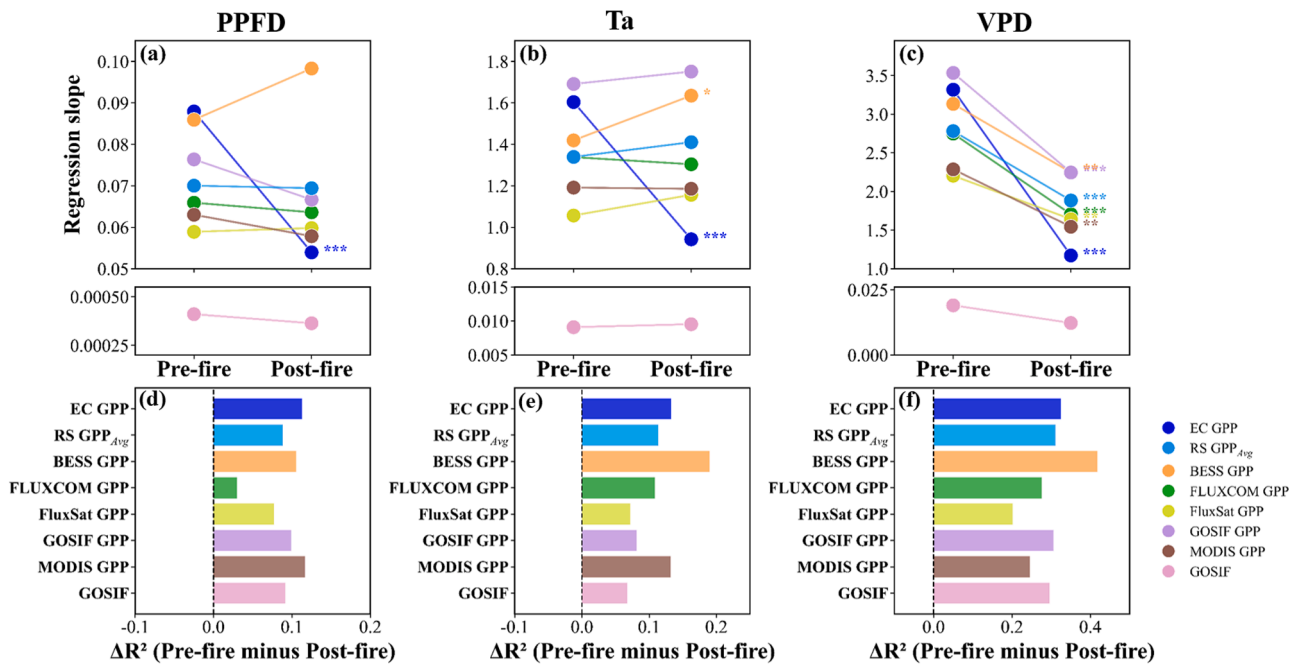
12

Fig. 11. Fire-induced shifts in the sensitivity of 8-day GPP to meteorological drivers at US-Vcm (forest site). (a–c) show the regression slopes (sensitivity) of GPP to PPFD (a), Ta (b), and VPD (c) before and after fire, while (d–f) present the changes in R^2 between the pre- and post-fire periods (pre-fire minus post-fire). Asterisks indicate statistical significance levels for pre- vs. post-fire differences ($*p < 0.05$, $**p < 0.01$, $***p < 0.001$).

estimates that were relatively close to EC GPP, several satellite products (e.g., MODIS, FLUXCOM, FluxSat) signaled recovery within only a few months (Fig. 9a–b). It is worth noting that EC GPP exhibited high recovery rates (RecR) because absolute flux values were very low immediately after fire, leading to steep relative growth (Fig. 9c–d). Moreover, EC GPP showed slow and gradual carbon uptake after fire, and its lower accumulated GPP was also a consequence of the lowered post-fire baseline. In contrast, satellite products maintained higher post-fire baselines, resulting in lower RecR despite showing faster recovery in terms of TTR and accumulated GPP. This apparent discrepancy highlights that "recovery speed" depends on the metric used: EC GPP captured rapid relative growth from a depressed baseline but still accumulated less carbon overall, whereas satellite products signaled premature recovery in timing and magnitude but underestimated relative growth rates. Differences among satellite GPP products likely reflect their structural assumptions. MODIS GPP directly scales productivity with APAR and LUE, so canopy regreening is often interpreted as functional recovery (Running et al., 2004; Zhang et al., 2017), leading to premature carbon gain. BESS GPP includes more explicit physiological constraints and thus capture recovery timing better, but they assume fixed climate—photosynthesis responses and consequently overestimate accumulated GPP (Jiang and Ryu, 2016; Ryu et al., 2011). Machine learning products (FLUXCOM and FluxSat) extrapolate recovery from undisturbed training data, leading to unrealistically short TTR under disturbance (Barnes et al., 2021; Gaber et al., 2024).

These discrepancies were not limited to GPP products. The reconstructed SIF dataset (GOSIF) showed performance patterns largely consistent with GOSIF GPP, since the latter is derived through biome-specific scaling of GOSIF (Li and Xiao, 2019b). For fire-induced loss, both captured immediate strong declines, closer to EC GPP than structural indices, confirming the functional sensitivity of SIF (Fig. 6). During recovery, GOSIF tracked the timing of rebound relatively well, with TTR estimates comparable to EC GPP (Fig. 9). However, similar to GPP products, GOSIF underestimated the long-term GPP suppression during the recovery period, suggesting overly fast recovery. This is consistent with a recent study which reported post-fire mismatches between satellite-derived SIF and EC-based GPP in Australian eucalypt forests,

where SIF underestimated recovery duration (Woodgate et al., 2025). Overall, GOSIF provides a physiologically meaningful signal and complements GPP products by more directly capturing photosynthetic responses, while its reconstruction framework may smooth some disturbance dynamics.

Structural proxies showed systematic biases that help explain inconsistencies in satellite GPP models, since NIRv, LAI, or related vegetation indices are fundamental inputs across model families. For fire-induced loss, they underestimated MRD and MRC (Fig. 6), as greenness and canopy area can persist despite sharp reductions in photosynthetic activity. During recovery, NIRv rebounded rapidly, often returning to pre-fire levels well before EC GPP, thus signaling premature recovery (Fig. 9). LAI showed weaker sensitivity to immediate fire loss and a slower rebound in grass/shrub ecosystems, reflecting its dependence on gradual canopy rebuilding (Lv et al., 2025), though results were not evaluated for forests. Greenness-sensitive indicators (e.g., NIRv) may overestimate recovery (Guo et al., 2021; Yan et al., 2025), while LAI may smooth or damp recovery signals (Shi et al., 2025), and these tendencies ultimately propagate into GPP products. In contrast, models that combine both structural and functional constraints (e.g., BESS GPP, GOSIF GPP) produced recovery times more consistent with EC GPP than those relying on a single structural predictor.

Overall, remote sensing proxies captured the direction of fire impacts but showed systematic biases in magnitude and recovery. Among these products, BESS GPP and GOSIF performed relatively better, providing closer estimates of immediate loss and recovery timing compared with EC GPP, though they still underestimated persistent suppression and tended to overestimate cumulative carbon gain. MODIS GPP showed intermediate performance, detecting strong fire-induced loss but portraying recovery too rapidly in forests. Machine learning products (FluxSat, FLUXCOM) were least reliable, consistently underestimating loss and exaggerating recovery speed, reflecting their limited capacity to extrapolate disturbance dynamics beyond training data (Barnes et al., 2021; Gaber et al., 2024). Structural proxies further explained these discrepancies: NIRv rebounded too quickly, signaling premature recovery, while LAI showed limited sensitivity to fire-induced loss and only partial consistency during recovery in grass/shrub ecosystems.

Taken together, proxies with physiological or process-based foundations are more reliable for tracking post-fire GPP trajectories, yet all systematically underestimated persistent suppression and overestimated long-term carbon gain, particularly in forests.

4.2. Ecosystem-type contrast: forest vs. grass/shrub

Wildfire impacts and recovery trajectories differed strongly between forests and grass/shrub ecosystems. Forests experienced far more severe fire-induced GPP loss and much slower recovery, whereas grass and shrub sites sustained smaller losses and recovered within months. This finding is consistent with global-scale studies showing a positive relationship between the magnitude of fire-induced loss and the time required for recovery (Xu et al., 2024). EC flux tower observations indicated that post-fire reductions in GPP for forests were approximately three times greater than those for grass/shrub sites (Fig. 6), with TTR extended by ~300 days (Fig. 9). In addition, RecR of grass and shrub sites were about twice as high as those of forests (Fig. 9). These differences primarily reflect fundamental ecosystem characteristics. Forests, with high baseline productivity, complex vertical structure, and substantial fuel loads, are prone to high-intensity crown fires that cause widespread canopy mortality and prolonged physiological impairment, requiring years to decades for biomass and canopy layers to rebuild (Bonner et al., 2024; Hakkenberg et al., 2024; Parks et al., 2014). In contrast, grass and shrub ecosystems, with lower baseline biomass, typically experience less severe damage and benefit from reduced competition for resources after fire, enabling rapid regrowth of surviving vegetation and establishment of new individuals (Ermitão et al., 2024; Pan et al., 2025; Xu et al., 2024).

Remote sensing products generally reproduced these ecosystem-type contrasts, but biases were much larger in forests than in grass/shrub ecosystems. In forests, most proxies underestimated persistent suppression (MRC), overestimated accumulated GPP, and produced shorter TTRs than EC GPP, signaling premature recovery (Fig. 6–9). These discrepancies might arise from several factors. First, spectral contamination from residual deadwood and charred debris introduces non-photosynthetic signals, reducing the accuracy of reflectance-based indices such as NIRv and LAI (Lewis et al., 2007; Yang and Guo, 2014). Because many satellite GPP models use these structural proxies as key inputs (Wang et al., 2021; Wu et al., 2011; J. Xu et al., 2025), their biases propagate into GPP products and exacerbate recovery overestimation. Second, post-fire regeneration is highly heterogeneous, with understory plants or saplings restoring greenness well before canopy photosynthetic capacity recovers (Celebrezze et al., 2024; Lopes et al., 2024; Woodgate et al., 2025), causing functional recovery to be overestimated. Third, fire altered the climate sensitivity of forest GPP, as EC observations showed weakened responses to PPFD, Ta, and VPD after fire, while satellite products failed to capture these shifts (Fig. 11). This shift likely reflects fire-induced canopy loss and physiological impairment, which reduce leaf area and active photosynthetic capacity, thereby weakening ecosystem responses to light, temperature, and VPD (Huang et al., 2020; Wolf et al., 2021; Zheng et al., 2024). In contrast, grass/shrub ecosystems—where recovery is rapid and dominated by resprouting or fast-growing species—maintained relatively stable climate—GPP coupling, and satellite products were able to track EC GPP more consistently.

To further assess whether ecosystem-type differences were influenced by fire severity, we stratified all flux tower sites by RdNBR. In grass/shrub ecosystems, the agreement between remote sensing proxies and EC GPP remained broadly consistent across low- and moderate-severity fires (Fig. S14–15). In contrast, forest sites showed weaker overall agreement (Fig. S16–17), with the largest satellite–EC discrepancies occurring after low-severity burns (Fig. S16). One likely explanation is that moderate-severity fires generate more distinct canopy disturbances that are more easily detected by satellite products (Dixon et al., 2023), whereas low-severity fires induce only subtle changes in

canopy or surface conditions that are difficult for remote sensing to capture accurately (Arnett et al., 2015; Epting et al., 2005). Additionally, post-fire data gaps at some forest sites limited further comparisons of recovery time, recovery rate, and GPP sensitivity to meteorological drivers.

In summary, forests not only suffered greater fire-induced suppression but also exhibited larger discrepancies between remote sensing proxies and flux observations, possibly due to structural complexity, spectral contamination, heterogeneous regeneration, and altered climate sensitivity. By contrast, grass and shrub systems recovered faster and more homogeneously, with satellite products tracking their dynamics more reliably. These results highlight the particular challenge of monitoring forest recovery with current satellite proxies, and underscore the need for functional indicators and disturbance-responsive models tailored for complex forest systems.

4.3. Uncertainties and implications in post-fire carbon monitoring

Beyond ecosystem-type contrasts, our study also has methodological limitations that should be acknowledged. The main constraints arise from the spatio-temporal resolution of satellite products, uncertainties inherent in EC data and the limited number and heterogeneity of EC sites.

Spatial resolution was tested using MODIS GPP, the only product with native 500 m resolution. Comparisons across 0.05°, 500 m, and 1000 m grids showed that spatial resolution had little influence on fire-induced loss or recovery metrics (Fig. 12). Temporal resolution was evaluated by comparing 8-day and monthly aggregated data for all products. The patterns of proxy—EC differences were robust across temporal scales (Fig. 13): remote sensing consistently underestimated MRC, MRD, and TTR relative to EC GPP, with larger discrepancies in forests than in grass/shrub ecosystems. For RecR, proxies also underestimated recovery rates, but the relative bias was larger in grass/shrub sites, likely because their higher EC RecR values amplified differences. These consistent patterns across temporal resolutions confirm that our central conclusions—systematic underestimation of fire impacts and recovery time by satellite proxies, and stronger biases in forests for most metrics—are not sensitive to temporal aggregation.

Uncertainties in EC-derived GPP may arise from turbulence conditions, flux partitioning, and energy balance closure, all of which can be influenced by post-fire structural changes. The EC technique assumes homogeneous terrain and stationary wind fields (Baldocchi, 2003; Barcza et al., 2009; Griebel et al., 2016), and canopy loss can modify surface roughness and local turbulence (Karna et al., 2020; Meyers et al., 2025). However, our wind-field analyses (Fig. S18) show that wind direction and wind-speed distributions remained broadly similar before and after fire at nearly all sites. The only notable shift occurred at AU-Wac, where lower post-fire wind speeds were due to the flux tower being replaced after the 2009 fire (from 100 m to a 5 m structure above the recovering canopy) rather than changes in turbulence (Qiu et al., 2026). Methodological uncertainties from flux partitioning were also small: daytime- and nighttime-based GPP estimates were highly consistent (Fig. S19), and a sensitivity analysis using an alternative partitioning approach (Fig. S20) yielded satellite–EC relationships closely aligned with those in the main analysis. Energy balance closure was likewise stable, with pre-fire values ranging ~0.72–0.91 in forests and ~0.58–0.88 in grass/shrub sites, and post-fire values remaining within similar ranges (Fig. S21). The mean change across sites (|mean ΔEBC| = 0.04 ± 0.03), with no systematic degradation following disturbance. Taken together, these diagnostics indicate that although EC measurements carry inherent uncertainties, wildfire did not introduce consistent biases in turbulence, partitioning, or closure, and thus the relative temporal patterns in EC GPP used to benchmark satellite proxies remain robust.

A further limitation is the restricted number of flux sites with complete pre- and post-fire records (n = 10). We searched all publicly
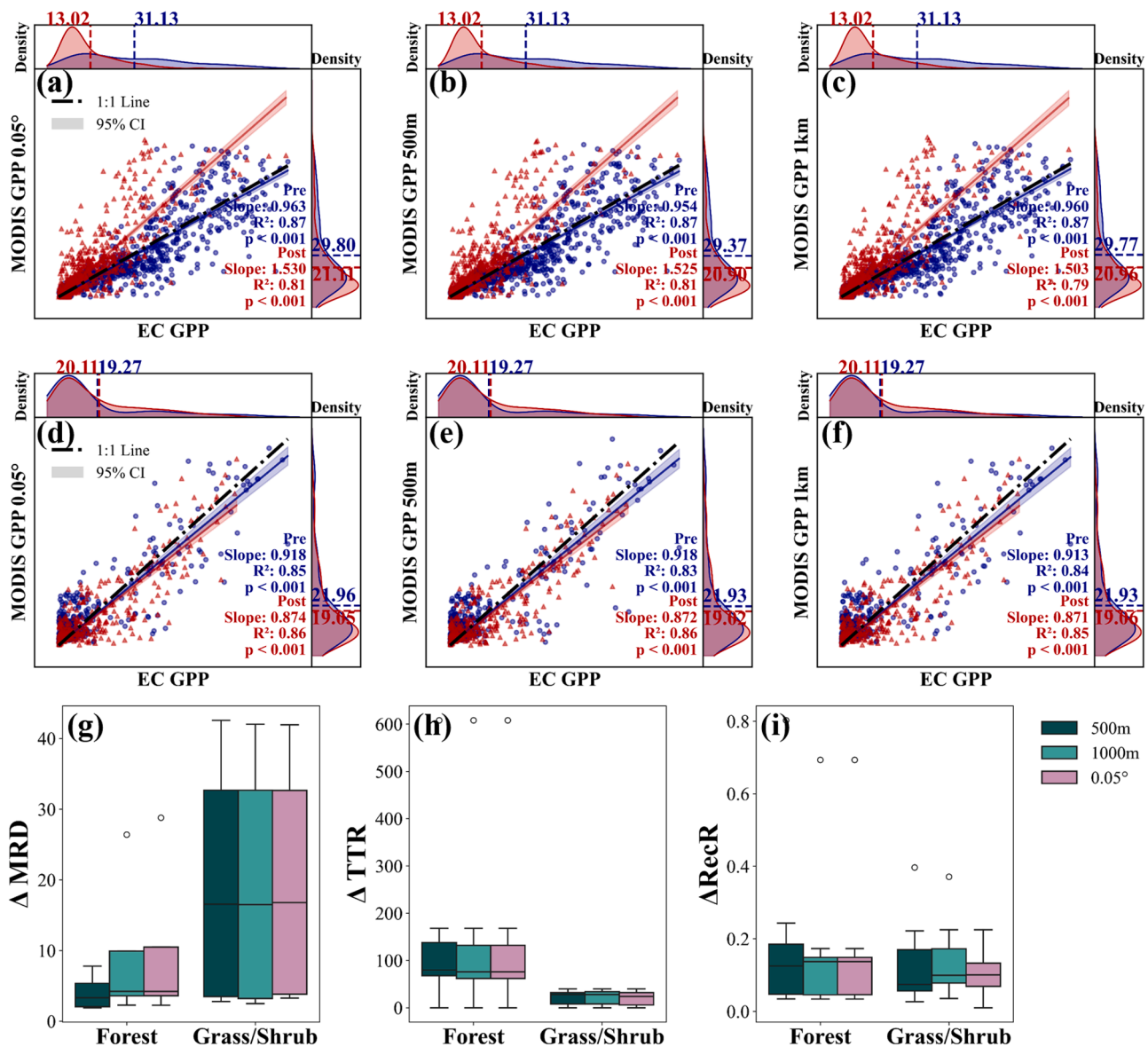
Fig. 12. Evaluation of spatial resolution effects on post-fire GPP dynamics. Relationships between MODIS GPP and EC GPP at forest sites under three spatial resolutions: 0.05° (a), 500 m (b), and 1000 m (c), separated into pre-fire (blue) and post-fire (red) periods. Corresponding relationships for grass/shrub sites are shown at 0.05° (d), 500 m (e), and 1000 m (f). Differences (Δ) in post-fire metrics between MODIS and EC GPP are summarized for maximum relative decrease (MRD) (g), time to recovery (TTR) (h), and recovery rate (RecR) (i).

available eddy covariance databases worldwide, yet only these sites provided continuous long-term observations that spanned both pre-fire and post-fire periods. This highlights the extreme scarcity of flux measurements capturing the full disturbance–recovery cycle, which constrains the generalizability of our results. In addition, substantial inter-site variability was observed, reflecting differences in fire severity, vegetation composition, and ecosystem condition. For example, while most forest sites showed clear overestimation of accumulated GPP by remote sensing products, AU-Cpr was an exception where proxies closely matched EC GPP (Fig. 7,8), likely because it represents a mallee woodland characterized by relatively low tree cover and sparse leaf canopies (Sun and Marschner, 2024). Such heterogeneity emphasizes that our findings represent general patterns across ecosystems rather than site-specific outcomes. Future progress will require expanding flux tower coverage in fire-prone regions, incorporating a wider range of fire regimes and severities, and integrating these benchmarks with satellite evaluations to test the robustness of global assessments.

Despite these limitations, our study provides the first cross-product

evaluation anchored in flux observations across multiple fire-affected sites, establishing general patterns of post-fire biases that can guide the interpretation of satellite proxies. Looking forward, improving post-fire monitoring will require several advances. First, expanding the flux tower network in fire-prone regions, complemented by ancillary measurements targeting wind field alterations and canopy structural heterogeneity, is crucial for quantifying and correcting flux data uncertainties in disturbed ecosystems (Bu and Xiao, 2025; Chen et al., 2024; Han et al., 2021). Second, multi-source integration—linking direct SIF retrievals, structural metrics (e.g., NIRv, LAI), and process-based models—offers a pathway to reduce biases and better capture both canopy structure and physiological function during recovery (Guan et al., 2025; Liu et al., 2025). Third, developing disturbance-responsive models that dynamically adjust productivity–climate relationships will be critical for reflecting physiological impairment and altered sensitivities after fire (Ren et al., 2025). Ultimately, addressing these gaps will reduce uncertainties in carbon budget assessments, improve projections of land–climate feedbacks, and
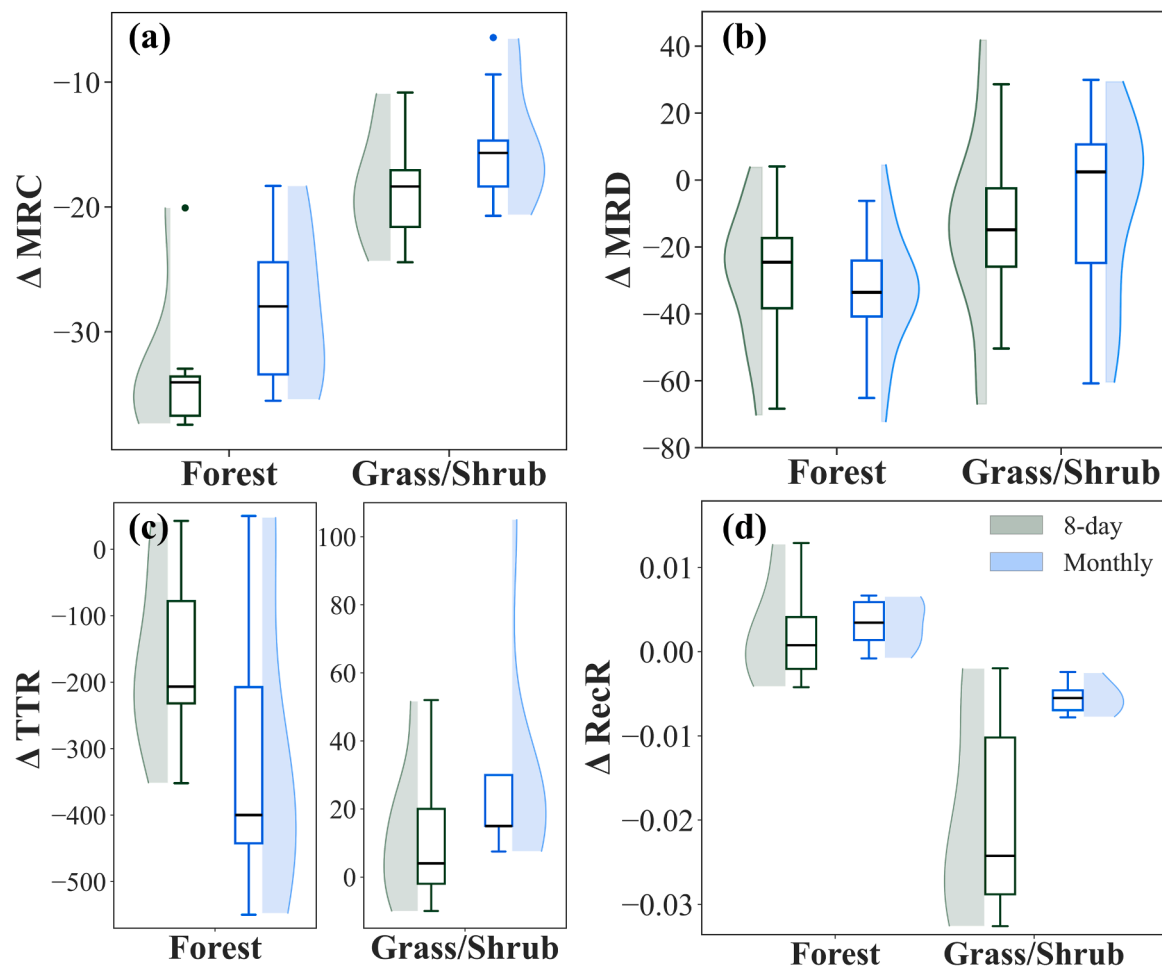
Fig. 13. Evaluation of temporal resolution effects on post-fire GPP dynamics. Differences (Δ) between remote sensing proxies and EC GPP are shown for mean relative change (MRC) (a), maximum relative decrease (MRD) (b), time to recovery (TTR) (c), and recovery rate (RecR) (d), comparing 8-day and monthly aggregated data.

provide a stronger scientific basis for managing fire-affected ecosystems under a warming and increasingly fire-prone world.

5. Conclusions

This study assessed the performance of five satellite-derived GPP products (BESS GPP, FLUXCOM GPP, FluxSat GPP, GOSIF GPP, MODIS GPP) and three complementary proxies (GOSIF, LAI, NIRv) against flux tower observations across forest and grass/shrub ecosystems affected by wildfire. Several consistent patterns emerged. First, satellite proxies captured the direction of fire impacts but systematically underestimated carbon loss: MRD of EC GPP exceeded 90 % in forests, whereas satellite products reported substantially smaller declines. Persistent suppression was also underestimated, as reflected by lower MRC compared with EC. Second, during recovery, satellite products generally overestimated carbon gain, with cumulative post-fire GPP substantially higher than EC, particularly in forests. This divergence was associated with shorter TTR and slower recovery rates RecR in satellite products, which signaled premature recovery relative to flux observations. Third, ecosystem contrasts were pronounced: forests showed greater GPP loss, slower recovery, and larger satellite–EC discrepancies, whereas grass and shrub ecosystems rebounded more quickly and were tracked more consistently by remote sensing. Among these products, BESS GPP and GOSIF provided relatively better estimates of immediate loss and recovery timing, though they still overestimated long-term recovery magnitude. Finally, EC data revealed marked post-fire reductions in GPP–climate sensitivity

in forests, which were not captured by satellite proxies. Together, these findings highlight both the potential and the limitations of current satellite proxies for monitoring post-fire carbon fluxes. Future progress will require improved models that incorporate disturbance-responsive processes, expanded ground-based measurements in fire-prone regions, and greater use of functional indicators such as SIF to better capture physiological constraints and ecosystem-specific recovery dynamics.

CRediT authorship contribution statement

Xinyi Fan: Writing – original draft, Visualization, Software, Methodology, Formal analysis, Data curation, Conceptualization. **Qinggaozi Zhu:** Writing – review & editing, Supervision, Data curation. **Yingnan Wei:** Data curation. **Ning Yao:** Writing – review & editing. **Gang Zhao:** Writing – review & editing. **Qiang Yu:** Writing – review & editing, Supervision. **Genghong Wu:** Writing – review & editing, Writing – original draft, Supervision, Project administration, Methodology, Formal analysis, Conceptualization.

Declaration of competing interest

The authors declare that they have no known competing financial interests or personal relationships that could have appeared to influence the work reported in this paper.

Acknowledgements

Supplementary materials

Supplementary material associated with this article can be found, in the online version, at doi:10.1016/j.agrformet.2025.110963.

Data availability

Data will be made available on request.

References

Andela, N., Morton, D.C., Giglio, L., Chen, Y., van der Werf, G.R., Kasibhatla, P.S., DeFries, R.S., Collatz, G.J., Hantson, S., Kloster, S., Bachelet, D., Forrest, M., Lasslop, G., Li, F., Mangeon, S., Melton, J.R., Yue, C., Randerson, J.T., 2017. A human-driven decline in global burned area. Science 356, 1356–1362. https://doi.org/10.1126/science.aal4108.

Arnett, J.T., Coops, N.C., Daniels, L.D., Falls, R.W., 2015. Detecting forest damage after a low-severity fire using remote sensing at multiple scales. Int. J. Appl. Earth Obs. Geoinformation 35, 239–246.

Ba, R., Lovallo, M., Song, W., Zhang, H., Telesca, L., 2022. Multifractal analysis of MODIS Aqua and Terra Satellite time series of normalized difference vegetation index and enhanced vegetation index of sites affected by wildfires. Entropy 24, 1748. https://doi.org/10.3390/e24121748.

Badgley, G., Anderegg, L.D.L., Berry, J.A., Field, C.B., 2019. Terrestrial gross primary production: using NIRV to scale from site to globe. Glob. Change Biol. 25, 3731–3740. https://doi.org/10.1111/gcb.14729.

Badgley, G., Field, C.B., Berry, J.A., 2017. Canopy near-infrared reflectance and terrestrial photosynthesis. Sci. Adv. 3, e1602244. https://doi.org/10.1126/sciadv.1602244.

Baldocchi, D., Novick, K., Keenan, T., Torn, M., 2024. AmeriFlux: its impact on our understanding of the 'breathing of the biosphere', after 25 years. Agric. For. Meteorol. 348, 109929. https://doi.org/10.1016/j.agrformet.2024.109929.

Baldocchi, D.D., 2003. Assessing the eddy covariance technique for evaluating carbon dioxide exchange rates of ecosystems: past, present and future. Glob. Change Biol. 9, 479–492.

Bandopadhyay, S., Sánchez, D.A.C., 2020. Amazonian fire events disturbed the global carbon cycle: a study from 2019 Amazon wildfire using Google Earth engine. Environ. Sci. Proc. 3, 43. https://doi.org/10.3390/IECF2020-08033.

Barcza, Z., Kern, A., Haszpra, L., Kljun, N., 2009. Spatial representativeness of tall tower eddy covariance measurements using remote sensing and footprint analysis. Agric. For. Meteorol. 149, 795–807.

Barnes, M.L., Farella, M.M., Scott, R.L., Moore, D.J.P., Ponce-Campos, G.E., Biederman, J.A., MacBean, N., Litvak, M.E., Breshears, D.D., 2021. Improved dryland carbon flux predictions with explicit consideration of water-carbon coupling. Commun. Earth Environ. 2, 248. https://doi.org/10.1038/s43247-021-00308-2.

Bastos, A., Gouveia, C.M., DaCamara, C.C., Trigo, R.M., 2011. Modelling post-fire vegetation recovery in Portugal. Biogeosciences 8, 3593–3607.

Baur, M.J., Friend, A.D., Pellegrini, A.F.A., 2024. Widespread and systematic effects of fire on plant–soil water relations. Nat. Geosci. 17, 1115–1120. https://doi.org/10.1038/s41561-024-01563-6.

Beringer, J., Hutley, L.B., McHugh, I., Arndt, S.K., Campbell, D., Cleugh, H.A., Cleverly, J., Resco de Dios, V., Eamus, D., Evans, B., Ewenz, C., Grace, P., Griebel, A., Haverd, V., Hinko-Najera, N., Huete, A., Isaac, P., Kanniah, K., Leuning, R., Liddell, M.J., Macfarlane, C., Meyer, W., Moore, C., Pendall, E., Phillips, A., Phillips, R.L., Prober, S.M., Restrepo-Coupe, N., Rutledge, S., Schroder, I., Silberstein, R., Southall, P., Yee, M.S., Tapper, N.J., van Gorsel, E., Vote, C., Walker, J., Wardlaw, T., 2016. An introduction to the Australian and New Zealand flux tower network – OzFlux. Biogeosciences 13, 5895–5916. https://doi.org/10.5194/bg-13-5895-2016.

Bonner, S.R., Hoffman, C.M., Linn, R.R., Tinkham, W.T., Atchley, A.L., Sieg, C.H., Varner, J.M., O'Brien, J.J., Hiers, J.K., 2024. Forest structural complexity and ignition pattern influence simulated prescribed fire effects. Fire Ecol 20, 82. https://doi.org/10.1186/s42408-024-00314-7.

Bradstock, R.A., 2010. A biogeographic model of fire regimes in Australia: current and future implications. Glob. Ecol. Biogeogr. 19, 145–158. https://doi.org/10.1111/j.1466-8238.2009.00512.x.

Bu, J., Xiao, J., 2025. Upscaling eddy covariance measurements of carbon and water fluxes to the continental scale by incorporating GEDI-derived canopy structural complexity metrics. Remote Sens. Environ. 329, 114930. https://doi.org/10.1016/j.rse.2025.114930.

Burton, C.A., Kelley, D.I., Burke, E., Mathison, C., Jones, C.D., Betts, R.A., Robertson, E., Teixeira, J.C.M., Cardoso, M., Anderson, L.O., 2024. Fire weakens land carbon sinks before 1.5 °C. Nat. Geosci. 17, 1108–1114. https://doi.org/10.1038/s41561-024-01554-7.

Canadell, J.G., Meyer, C.P.(Mick), Cook, G.D., Dowdy, A., Briggs, P.R., Knauer, J., Pepler, A., Haverd, V., 2021. Multi-decadal increase of forest burned area in Australia is linked to climate change. Nat. Commun. 12, 6921. https://doi.org/10.1038/s41467-021-27225-4.

Celebrezze, J.V., Franz, M.C., Andrus, R.A., Stahl, A.T., Steen-Adams, M., Meddens, A.J.H., 2024. A fast spectral recovery does not necessarily indicate post-fire forest recovery. Fire Ecol 20, 54. https://doi.org/10.1186/s42408-024-00288-6.

Chen, Y., Hall, J., van Wees, D., Andela, N., Hantson, S., Giglio, L., van der Werf, G.R., Morton, D.C., Randerson, J.T., 2023. Multi-decadal trends and variability in burned area from the fifth version of the Global Fire Emissions Database (GFED5). Earth Syst. Sci. Data 15, 5227–5259. https://doi.org/10.5194/essd-15-5227-2023.

Chen, Y., Morton, D.C., Randerson, J.T., 2024. Remote sensing for wildfire monitoring: insights into burned area, emissions, and fire dynamics. One Earth 7, 1022–1028. https://doi.org/10.1016/j.oneear.2024.05.014.

Dixon, D.J., Zhu, Y., Brown, C.F., Jin, Y., 2023. Satellite detection of canopy-scale tree mortality and survival from California wildfires with spatio-temporal deep learning. Remote Sens. Environ. 298, 113842. https://doi.org/10.1016/j.rse.2023.113842.

Epting, J., Verbyla, D., Sorbel, B., 2005. Evaluation of remotely sensed indices for assessing burn severity in interior Alaska using Landsat TM and ETM+. Remote Sens. Environ. 96, 328–339.

Ermitão, T., Gouveia, C.M., Bastos, A., Russo, A.C., 2024. Recovery following recurrent fires across Mediterranean ecosystems. Glob. Change Biol. 30, e70013. https://doi.org/10.1111/gcb.70013.

Fan, L., Wigneron, J.-P., Ciais, P., Chave, J., Brandt, M., Sitch, S., Yue, C., Bastos, A., Li, Xin, Qin, Y., Yuan, W., Schepaschenko, D., Mukhortova, L., Li, Xiaojun, Liu, X., Wang, M., Frappart, F., Xiao, X., Chen, J., Ma, M., Wen, J., Chen, X., Yang, H., van Wees, D., Fensholt, R., 2023. Siberian carbon sink reduced by forest disturbances. Nat. Geosci. 16, 56–62. https://doi.org/10.1038/s41561-022-01087-x.

Flannigan, M., Cantin, A.S., De Groot, W.J., Wotton, M., Newbery, A., Gowman, L.M., 2013. Global wildland fire season severity in the 21st century. For. Ecol. Manag. 294, 54–61. https://doi.org/10.1016/j.foreco.2012.10.022.

Frankenberg, C., Fisher, J.B., Worden, J., Badgley, G., Saatchi, S.S., Lee, J.-E., Toon, G.C., Butz, A., Jung, M., Kuze, A., Yokota, T., 2011. New global observations of the terrestrial carbon cycle from GOSAT: patterns of plant fluorescence with gross primary productivity. Geophys. Res. Lett. 38. https://doi.org/10.1029/2011GL048738.

Gaber, M., Kang, Y., Schurgers, G., Keenan, T., 2024. Using automated machine learning for the upscaling of gross primary productivity. Biogeosciences 21, 2447–2472. https://doi.org/10.5194/bg-21-2447-2024.

Griebel, A., Bennett, L.T., Metzen, D., Cleverly, J., Burba, G., Arndt, S.K., 2016. Effects of inhomogeneities within the flux footprint on the interpretation of seasonal, annual, and interannual ecosystem carbon exchange. Agric. For. Meteorol. 221, 50–60. https://doi.org/10.1016/j.agrformet.2016.02.002.

Gu, X., Zhou, L., Liang, Q., Xu, L., 2025. Biome-specific responses of GOSIF gross primary productivity to wildfires in South America. J. Geophys. Res. Biogeosciences 130, e2025JG008986. https://doi.org/10.1029/2025JG008986.

Guan, X., Li, Y., Chen, J.M., Ma, Y., Shen, H., 2025. A process model-guided transfer learning framework for mapping global gross primary production. Agric. For. Meteorol. 372, 110678. https://doi.org/10.1016/j.agrformet.2025.110678.

Gui, Y., Wang, K., Huntingford, C., Wei, S., Li, X., Myneni, R.B., Piao, S., 2025. Vegetation greenness in 2024. Nat. Rev. Earth Environ. 6, 255–257. https://doi.org/10.1038/s43017-025-00656-z.

Gülci, S., Wing, M.G., 2025. Evaluating forest fire severity and vegetative recovery using Sentinel imagery and spectral indices in a cloud-based environment. Adv. Space Res. https://doi.org/10.1016/j.asr.2025.07.044.

Guo, M., Li, J., Yu, F., Yin, S., Huang, S., Wen, L., 2021. Estimation of post-fire vegetation recovery in boreal forests using solar-induced chlorophyll fluorescence (SIF) data. Int. J. Wildland Fire 30, 365–377. https://doi.org/10.1071/WF20162.

Hakkenberg, C.R., Clark, M.L., Bailey, T., Burns, P., Goetz, S.J., 2024. Ladder fuels rather than canopy volumes consistently predict wildfire severity even in extreme topographic-weather conditions. Commun. Earth Environ. 5, 721. https://doi.org/10.1038/s43247-024-01893-8.

Han, D., Di, X., Yang, G., Sun, L., Weng, Y., 2021. Quantifying fire severity: a brief review and recommendations for improvement. Ecosyst. Health Sustain.

Haxeltine, A., Prentice, I.C., 1996. A general model for the light-use efficiency of primary production. Funct. Ecol. 10, 551–561. https://doi.org/10.2307/2390165.

Hemes, K.S., Norlen, C.A., Wang, J.A., Goulden, M.L., Field, C.B., 2023. The magnitude and pace of photosynthetic recovery after wildfire in California ecosystems. Proc. Natl. Acad. Sci. 120, e2201954120. https://doi.org/10.1073/pnas.2201954120.

Huang, H., Xue, Y., Li, F., Liu, Y., 2020. Modeling long-term fire impact on ecosystem characteristics and surface energy using a process-based vegetation–fire model SSiB4/TRIFFID-Fire v1.0. Geosci. Model Dev 13, 6029–6050. https://doi.org/10.5194/gmd-13-6029-2020.

Huang, S., Liu, H., Dahal, D., Jin, S., Welp, L.R., Liu, J., Liu, S., 2013. Modeling spatially explicit fire impact on gross primary production in interior Alaska using satellite images coupled with eddy covariance. Remote Sens. Environ. 135, 178–188. https://doi.org/10.1016/j.rse.2013.04.003.

Huang, X., Xue, L., Wang, Z., Liu, Y., Ding, K., Ding, A., 2024. Escalating wildfires in Siberia driven by climate feedbacks under a warming Arctic in the 21st century. AGU Adv 5, e2023AV001151. https://doi.org/10.1029/2023AV001151.

Hung, J.K.Y., Arndt, K.A., Murphy, P., Montemayor, M., Rodenhizer, H., Ludwig, S., Rogers, B.M., Natali, S.M., 2024. Slow post-fire carbon balance recovery despite increased net uptake rates in Alaskan tundra. Environ. Res. Lett. 19, 124013. https://doi.org/10.1088/1748-9326/ad8764.

Isaac, P., Cleverly, J., McHugh, I., Van Gorsel, E., Ewenz, C., Beringer, J., 2017. OzFlux data: network integration from collection to curation. Biogeosciences 14, 2903–2928.

Jiang, C., Ryu, Y., 2016. Multi-scale evaluation of global gross primary productivity and evapotranspiration products derived from breathing Earth System Simulator (BESS). Remote Sens. Environ. 186, 528–547. https://doi.org/10.1016/j.rse.2016.08.030.

Joiner, J., Yoshida, Y., Zhang, Y., Duveiller, G., Jung, M., Lyapustin, A., Wang, Y., Tucker, C.J., 2018. Estimation of terrestrial global gross primary production (GPP) with satellite data-driven models and eddy covariance flux data. Remote Sens 10, 1346.

Jones, M.W., Kelley, D.I., Burton, C.A., Di Giuseppe, F., Barbosa, M.L.F., Brambleby, E., Hartley, A.J., Lombardi, A., Mataveli, G., McNorton, J.R., Spuler, F.R., Wessel, J.B., Abatzoglou, J.T., Anderson, L.O., Andela, N., Archibald, S., Armenteras, D., Burke, E., Carmenta, R., Chuvieco, E., Clarke, H., Doerr, S.H., Fernandes, P.M., Giglio, L., Hamilton, D.S., Hantson, S., Harris, S., Jain, P., Kolden, C.A., Kurvits, T., Lampe, S., Meier, S., New, S., Parrington, M., Perron, M.M.G., Qu, Y., Ribeiro, N.S., Saharjo, B.H., San-Miguel-Ayanz, J., Shuman, J.K., Tanpipat, V., van der Werf, G.R., Veraverbeke, S., Xanthopoulos, G., 2024. State of wildfires 2023–2024. Earth Syst. Sci. Data 16, 3601–3685. https://doi.org/10.5194/essd-16-3601-2024.

Jung, M., Schwalm, C., Migliavacca, M., Walther, S., Camps-Valls, G., Koirala, S., Anthoni, P., Besnard, S., Bodesheim, P., Carvalhais, N., Chevallier, F., Gans, F., Goll, D.S., Haverd, V., Köhler, P., Ichii, K., Jain, A.K., Liu, J., Lombardozzi, D., Nabel, J.E.M.S., Nelson, J.A., O'Sullivan, M., Pallandt, M., Papale, D., Peters, W., Pongratz, J., Rödenbeck, C., Sitch, S., Tramontana, G., Walker, A., Weber, U., Reichstein, M., 2020. Scaling carbon fluxes from eddy covariance sites to globe: synthesis and evaluation of the FLUXCOM approach. Biogeosciences 17, 1343–1365. https://doi.org/10.5194/bg-17-1343-2020.

Karna, Y.K., Penman, T.D., Aponte, C., Hinko-Najera, N., Bennett, L.T., 2020. Persistent changes in the horizontal and vertical canopy structure of fire-tolerant forests after severe fire as quantified using multi-temporal airborne lidar data. For. Ecol. Manag. 472, 118255. https://doi.org/10.1016/j.foreco.2020.118255.

Kelly, J., Kljun, N., Cai, Z., Doerr, S.H., D'Onofrio, C., Holst, T., Lehner, I., Lindroth, A., Thapa, S., Vestin, P., Santín, C., 2024. Wildfire impacts on the carbon budget of a managed Nordic boreal forest. Agric. For. Meteorol. 351, 110016. https://doi.org/10.1016/j.agrformet.2024.110016.

Kim, J.E., Wang, J.A., Li, Y., Czimczik, C.I., Randerson, J.T., 2024. Wildfire-induced increases in photosynthesis in boreal forest ecosystems of North America. Glob. Change Biol. 30, e17151. https://doi.org/10.1111/gcb.17151.

Lewis, S.A., Lentile, L.B., Hudak, A.T., Robichaud, P.R., Morgan, P., Bobbitt, M.J., 2007. Mapping ground cover using hyperspectral remote sensing after the 2003 Simi and old wildfires in Southern California. Fire Ecol 3, 109–128. https://doi.org/10.4996/fireecology.0301109.

Li, B., Ryu, Y., Jiang, C., Dechant, B., Liu, J., Yan, Y., Li, X., 2023. BESSv2.0: a satellite-based and coupled-process model for quantifying long-term global land–atmosphere fluxes. Remote Sens. Environ. 295, 113696. https://doi.org/10.1016/j.rse.2023.113696.

Li, X., Xiao, J., 2019a. A global, 0.05-degree product of solar-induced chlorophyll fluorescence derived from OCO-2, MODIS, and reanalysis data. Remote Sens 11, 517. https://doi.org/10.3390/rs11050517.

Li, X., Xiao, J., 2019b. Mapping photosynthesis solely from solar-induced chlorophyll fluorescence: a global, fine-resolution dataset of gross primary production derived from OCO-2. Remote Sens 11, 2563. https://doi.org/10.3390/rs11212563.

Liu, H., Ding, Q., Li, Y., Fan, L., Zhao, L., Ma, M., 2025. Improved biome-BGC model for simulating spatiotemporal dynamics of gross primary productivity in evergreen broadleaf forests of the karst region. Environ. Model. Softw. 192, 106563. https://doi.org/10.1016/j.envsoft.2025.106563.

Liu, J., Chen, J.M., Cihlar, J., Park, W.M., 1997. A process-based boreal ecosystem productivity simulator using remote sensing inputs. Remote Sens. Environ. 62, 158–175. https://doi.org/10.1016/S0034-4257(97)00089-8.

Lloyd, J., Taylor, J.A., 1994. On the temperature dependence of soil respiration. Funct. Ecol. 315–323.

Lopes, L.F., Dias, F.S., Fernandes, P.M., Acácio, V., 2024. A remote sensing assessment of oak forest recovery after postfire restoration. Eur. J. For. Res. 143, 1001–1014. https://doi.org/10.1007/s10342-024-01667-z.

Lv, Q., Chen, Z., Wu, C., Peñuelas, J., Fan, L., Su, Y., Yang, Z., Li, M., Gao, B., Hu, J., Zhang, C., Fu, Y., Wang, Q., 2025. Increasing severity of large-scale fires prolongs recovery time of forests globally since 2001. Nat. Ecol. Evol. 9, 980–992. https://doi.org/10.1038/s41559-025-02683-x.

Ma, H., Liang, S., 2022. Development of the GLASS 250-m leaf area index product (version 6) from MODIS data using the bidirectional LSTM deep learning model. Remote Sens. Environ. 273, 112985. https://doi.org/10.1016/j.rse.2022.112985.

Meyers, T.P., Krishnan, P., Heuer, M., Kochendorfer, J., Diamond, H.J., 2025. The impact of wildfire on the land surface parameters of a semi-arid grassland in the southwestern US. Agric. For. Meteorol. 363, 110390.

Miller, J.D., Thode, A.E., 2007. Quantifying burn severity in a heterogeneous landscape with a relative version of the delta normalized burn ratio (dNBR). Remote Sens. Environ. 109, 66–80. https://doi.org/10.1016/j.rse.2006.12.006.

Nelson, J.A., Walther, S., Gans, F., Kraft, B., Weber, U., Novick, K., Buchmann, N., Migliavacca, M., Wohlfahrt, G., Šigut, L., Ibrom, A., Papale, D., Göckede, M.,

Duveiller, G., Knohl, A., Hörtnagl, L., Scott, R.L., Dušek, J., Zhang, W., Hamdi, Z.M., Reichstein, M., Aranda-Barranco, S., Ardö, J., Op de Beeck, M., Billesbach, D., Bowling, D., Bracho, R., Brümmer, C., Camps-Valls, G., Chen, S., Cleverly, J.R., Desai, A., Dong, G., El-Madany, T.S., Euskirchen, E.S., Feigenwinter, I., Galvagno, M., Gerosa, G.A., Gielen, B., Goded, I., Goslee, S., Gough, C.M., Heinesch, B., Ichii, K., Jackowicz-Korczynski, M.A., Klosterhalfen, A., Knox, S., Kobayashi, H., Kohonen, K.-M., Korkiakoski, M., Mammarella, I., Gharun, M., Marzuoli, R., Matamala, R., Metzger, S., Montagnani, L., Nicolini, G., O'Halloran, T., Ourcival, J.-M., Peichl, M., Pendall, E., Ruiz Reverter, B., Roland, M., Sabbatini, S., Sachs, T., Schmidt, M., Schwalm, C.R., Shekhar, A., Silberstein, R., Silveira, M.L., Spano, D., Tagesson, T., Tramontana, G., Trotta, C., Turco, F., Vesala, T., Vincke, C., Vitale, D., Vivoni, E.R., Wang, Y., Woodgate, W., Yepez, E.A., Zhang, J., Zona, D., Jung, M., 2024. X-BASE: the first terrestrial carbon and water flux products from an extended data-driven scaling framework. FLUXCOM-X. Biogeosci. 21, 5079–5115. https://doi.org/10.5194/bg-21-5079-2024.

Pan, L., Xiao, X., Qin, Y., Canadell, J.G., Huete, A., Ciais, P., Yin, S., Zhang, C., Pan, B., Yin, C., Meng, C., Yao, Y., Xia, H., 2025. Strong and rapid postfire recovery of vegetation productivity in Australia. Glob. Change Biol. 31, e70321. https://doi.org/10.1111/gcb.70321.

Papale, D., Reichstein, M., Aubinet, M., Canfora, E., Bernhofer, C., Kutsch, W., Longdoz, B., Rambal, S., Valentini, R., Vesala, T., Yakir, D., 2006. Towards a standardized processing of Net Ecosystem Exchange measured with eddy covariance technique: algorithms and uncertainty estimation. Biogeosciences 3, 571–583. https://doi.org/10.5194/bg-3-571-2006.

Parks, S.A., Miller, C., Nelson, C.R., Holden, Z.A., 2014. Previous fires moderate burn severity of subsequent wildland fires in two large Western US wilderness areas. Ecosystems 17, 29–42. https://doi.org/10.1007/s10021-013-9704-x.

Phillips, C.A., Rogers, B.M., Elder, M., Cooperdock, S., Moubarak, M., Randerson, J.T., Frumhoff, P.C., 2022. Escalating carbon emissions from North American boreal forest wildfires and the climate mitigation potential of fire management. Sci. Adv. https://doi.org/10.1126/sciadv.abl7161.

Prentice, I.C., Balzarolo, M., Bloomfield, K.J., Chen, J.M., Dechant, B., Ghent, D., Janssens, I.A., Luo, X., Morfopoulos, C., Ryu, Y., Vicca, S., van Hoolst, R., 2024. Principles for satellite monitoring of vegetation carbon uptake. Nat. Rev. Earth Environ. 5, 818–832. https://doi.org/10.1038/s43017-024-00601-6.

Qiu, F., Zang, J., Zhang, Y., 2026. Divergent remote sensing signals in long-term post-fire eucalyptus recovery: structural vs. functional traits. Remote Sens. Environ. 333, 115121. https://doi.org/10.1016/j.rse.2025.115121.

Reichstein, M., Falge, E., Baldocchi, D., Papale, D., Aubinet, M., Berbigier, P., Bernhofer, C., Buchmann, N., Gilmanov, T., Granier, A., Grünwald, T., Havránková, K., Ilvesniemi, H., Janous, D., Knohl, A., Laurila, T., Lohila, A., Loustau, D., Matteucci, G., Meyers, T., Miglietta, F., Ourcival, J.-M., Pumpanen, J., Rambal, S., Rotenberg, E., Sanz, M., Tenhunen, J., Seufert, G., Vaccari, F., Vesala, T., Yakir, D., Valentini, R., 2005. On the separation of net ecosystem exchange into assimilation and ecosystem respiration: review and improved algorithm. Glob. Change Biol. 11, 1424–1439. https://doi.org/10.1111/j.1365-2486.2005.001002.x.

Ren, H., Zhang, L., Yan, M., Zhang, B., Ruan, L., 2025. Improving forest gross primary productivity estimation through climate and trait integration. Ecol. Model. 501.

Runge, K., Tucker, M., Crowther, T.W., Fournier de Laurière, C., Guirado, E., Bialic-Murphy, L., Berdugo, M., 2025. Monitoring terrestrial ecosystem resilience using earth observation data: identifying consensus and limitations across metrics. Glob. Change Biol. 31, e70115. https://doi.org/10.1111/gcb.70115.

Running, S.W., Nemani, R.R., Heinsch, F.A., Zhao, M., Reeves, M., Hashimoto, H., 2004. A continuous satellite-derived measure of global terrestrial primary production. BioScience 54, 547–560. https://doi.org/10.1641/0006-3568(2004)054%255B0547:ACSMOG%255D2.0.CO;2.

Ryu, Y., Baldocchi, D.D., Kobayashi, H., van Ingen, C., Li, J., Black, T.A., Beringer, J., van Gorsel, E., Knohl, A., Law, B.E., Roupsard, O., 2011. Integration of MODIS land and atmosphere products with a coupled-process model to estimate gross primary productivity and evapotranspiration from 1 km to global scales. Glob. Biogeochem. Cycles 25. https://doi.org/10.1029/2011GB004053.

Ryu, Y., Berry, J.A., Baldocchi, D.D., 2019. What is global photosynthesis? History, uncertainties and opportunities. Remote Sens. Environ. 223, 95–114. https://doi.org/10.1016/j.rse.2019.01.016.

Schimel, D., Pavlick, R., Fisher, J.B., Asner, G.P., Saatchi, S., Townsend, P., Miller, C., Frankenberg, C., Hibbard, K., Cox, P., 2015. Observing terrestrial ecosystems and the carbon cycle from space. Glob. Change Biol. 21, 1762–1776. https://doi.org/10.1111/gcb.12822.

Schoennagel, T., Balch, J.K., Brenkert-Smith, H., Dennison, P.E., Harvey, B.J., Krawchuk, M.A., Mietkiewicz, N., Morgan, P., Moritz, M.A., Rasker, R., Turner, M.G., Whitlock, C., 2017. Adapt to more wildfire in western North American forests as climate changes. Proc. Natl. Acad. Sci. 114, 4582–4590. https://doi.org/10.1073/pnas.1617464114.

Shakesby, R.A., Doerr, S.H., 2006. Wildfire as a hydrological and geomorphological agent. Earth-Sci. Rev. 74, 269–307. https://doi.org/10.1016/j.earscirev.2005.10.006.

Shen, Y., Prentice, I.C., Harrison, S.P., 2025. Investigation of factors that affect post-fire recovery of photosynthetic activity at global scale. Ecol. Indic. 171, 113206. https://doi.org/10.1016/j.ecolind.2025.113206.

Shi, M., McDowell, N., Huang, H., Zahura, F., Li, L., Chen, X., 2025. Ecosystem leaf area, gross primary production, and evapotranspiration responses to wildfire in the Columbia River basin. Biogeosciences 22, 2225–2238. https://doi.org/10.5194/bg-22-2225-2025.

Singh, S.S., Jeganathan, C., 2023. Quantifying forest resilience post forest fire disturbances using time-series satellite data. Environ. Monit. Assess. 196, 26. https://doi.org/10.1007/s10661-023-12183-9.

Srivastava, A., Suman, A., Biswas, S., 2025. Chapter 14 - assessment and monitoring of forest fire using vegetation indices and AI/ML techniques over google earth engine. Eds.. In: Sood, V., Gupta, D.K., Singh, S., Pradhan, B. (Eds.), Google Earth Engine and Artificial Intelligence For Earth Observation, Earth Observation. Elsevier, pp. 269–285. https://doi.org/10.1016/B978-0-443-27372-8.00005-2.

Sun, Q., Marschner, P., 2024. Severe wildfire increased variability in the response of gross primary production to climate in an eucalyptus dominated semi-arid woodland in South Australia. Agric. For. Meteorol. 355, 110142. https://doi.org/10.1016/j.agrformet.2024.110142.

Sun, Q., Meyer, W.S., Koerber, G.R., Marschner, P., 2020. Rapid recovery of net ecosystem production in a semi-arid woodland after a wildfire. Agric. For. Meteorol. 291, 108099. https://doi.org/10.1016/j.agrformet.2020.108099.

Tian, C., Yue, X., Zhu, J., Liao, H., Yang, Y., Lei, Y., Zhou, X., Zhou, H., Ma, Y., Cao, Y., 2022. Fire–climate interactions through the aerosol radiative effect in a global chemistry–climate–vegetation model. Atmospheric Chem. Phys. 22, 12353–12366. https://doi.org/10.5194/acp-22-12353-2022.

Tramontana, G., Jung, M., Schwalm, C.R., Ichii, K., Camps-Valls, G., Ráduly, B., Reichstein, M., Arain, M.A., Cescatti, A., Kiely, G., Merbold, L., Serrano-Ortiz, P., Sickert, S., Wolf, S., Papale, D., 2016. Predicting carbon dioxide and energy fluxes across global FLUXNET sites with regression algorithms. Biogeosciences 13, 4291–4313. https://doi.org/10.5194/bg-13-4291-2016.

Ueyama, M., Iwata, H., Nagano, H., Tahara, N., Iwama, C., Harazono, Y., 2019. Carbon dioxide balance in early-successional forests after forest fires in interior Alaska. Agric. For. Meteorol. 275, 196–207. https://doi.org/10.1016/j.agrformet.2019.05.020.

Walker, X.J., Baltzer, J.L., Cumming, S.G., Day, N.J., Ebert, C., Goetz, S., Johnstone, J.F., Potter, S., Rogers, B.M., Schuur, E.A.G., Turetsky, M.R., Mack, M.C., 2019. Increasing wildfires threaten historic carbon sink of boreal forest soils. Nature 572, 520–523. https://doi.org/10.1038/s41586-019-1474-y.

Wang, S., Zhang, Y., Ju, W., Qiu, B., Zhang, Z., 2021. Tracking the seasonal and inter-annual variations of global gross primary production during last four decades using satellite near-infrared reflectance data 755. https://doi.org/10.1016/j.scitotenv.2020.142569.

Wang, T., Zhang, Y., Yue, C., Wang, Y., Wang, X., Lyu, G., Wei, J., Yang, H., Piao, S., 2025. Progress and challenges in remotely sensed terrestrial carbon fluxes. Geo-Spat. Inf. Sci. 28, 1–21. https://doi.org/10.1080/10095020.2024.2336599.

Williams, R.J., Gill, A.M., Bradstock, R.A., 2012. Flammable Australia: fire regimes. Biodiversity and Ecosystems in a Changing World. Csiro Publishing.

Wine, M.L., Cadol, D., 2016. Hydrologic effects of large southwestern USA wildfires significantly increase regional water supply: fact or fiction? Environ. Res. Lett. 11, 085006. https://doi.org/10.1088/1748-9326/11/8/085006.

Wolf, K., Higuera, P., Davis, K., Dobrowski, S., 2021. Wildfire impacts on forest microclimate vary with biophysical context. Ecosphere 12. https://doi.org/10.1002/ecs2.3467.

Woodgate, W., Phinn, S., Devereux, T., Aryal, R.R., 2025. Bushfire recovery at a long-term tall eucalypt flux site through the lens of a satellite: combining multi-scale data for structural-functional insight. Remote Sens. Environ. 317, 114530. https://doi.org/10.1016/j.rse.2024.114530.

Wooster, M.J., Roberts, G.J., Giglio, L., Roy, D.P., Freeborn, P.H., Boschetti, L., Justice, C., Ichoku, C., Schroeder, W., Davies, D., Smith, A.M.S., Setzer, A., Csiszar, I., Strydom, T., Frost, P., Zhang, T., Xu, W., de Jong, M.C., Johnston, J.M., Ellison, L., Vadrevu, K., Sparks, A.M., Nguyen, H., McCarty, J., Tanpipat, V.,

Schmidt, C., San-Miguel-Ayanz, J., 2021. Satellite remote sensing of active fires: history and current status, applications and future requirements. Remote Sens. Environ 267, 112694. https://doi.org/10.1016/j.rse.2021.112694.

Wu, C., Chen, J.M., Huang, N., 2011. Predicting gross primary production from the enhanced vegetation index and photosynthetically active radiation: evaluation and calibration. Remote Sens. Environ. 115, 3424–3435. https://doi.org/10.1016/j.rse.2011.08.006.

Wu, T., Xu, L., Chen, N., 2024. Spatial pattern and attribution of ecosystem drought recovery in China. J. Hydrol. 638, 131578. https://doi.org/10.1016/j.jhydrol.2024.131578.

Xiao, J., Chevallier, F., Gomez, C., Guanter, L., Hicke, J.A., Huete, A.R., Ichii, K., Ni, W., Pang, Y., Rahman, A.F., Sun, G., Yuan, W., Zhang, L., Zhang, X., 2019. Remote sensing of the terrestrial carbon cycle: a review of advances over 50 years. Remote Sens. Environ. 233, 111383. https://doi.org/10.1016/j.rse.2019.111383.

Xu, H., Chen, H.W., Chen, D., Wang, Y., Yue, X., He, B., Guo, L., Yuan, W., Zhong, Z., Huang, L., Zheng, F., Li, T., He, X., 2024. Global patterns and drivers of post-fire vegetation productivity recovery. Nat. Geosci. 17, 874–881. https://doi.org/10.1038/s41561-024-01520-3.

Xu, J., Chen, T., Chen, X., Zhou, S., Gu, Z., Li, W., Cui, Y., Wang, S., Liu, S., 2025a. Estimating GPP in China using different site-level datasets, vegetation classification and vegetation indices. Ecol. Process. 14, 65. https://doi.org/10.1186/s13717-025-00617-w.

Xu, J., Cen, J., Fan, L., Liu, Y., Janssen, T.A.J., Liu, P., Wu, W., Wang, L., Li, N., Veraverbeke, S., 2025b. Land use and climatic drivers of early 21st-century fire activity in the Amazon. Agric. For. Meteorol. 372, 110664. https://doi.org/10.1016/j.agrformet.2025.110664.

Yan, Y., Hong, S., Chen, A., Peñuelas, J., Allen, C.D., Hammond, W.M., Munson, S.M., Myneni, R.B., Piao, S., 2025. Satellite-based evidence of recent decline in global forest recovery rate from tree mortality events. Nat. Plants 11, 731–742. https://doi.org/10.1038/s41477-025-01948-4.

Yang, X., Guo, X., 2014. Quantifying responses of spectral vegetation indices to dead materials in mixed grasslands. Remote Sens 6, 4289–4304. https://doi.org/10.3390/rs6054289.

Zhang, Y., Xiao, X., Wu, X., Zhou, S., Zhang, G., Qin, Y., Dong, J., 2017. A global moderate resolution dataset of gross primary production of vegetation for 2000–2016. Sci. Data 4, 170165. https://doi.org/10.1038/sdata.2017.165.

Zhao, J., Yue, C., Wang, J., Hantson, S., Wang, X., He, B., Li, G., Wang, L., Zhao, H., Luyssaert, S., 2024. Forest fire size amplifies postfire land surface warming. Nature 633, 828–834. https://doi.org/10.1038/s41586-024-07918-8.

Zheng, Y., Zhao, W., Chen, A., Chen, Y., Chen, J., Zhu, Z., 2024. Vegetation canopy structure mediates the response of gross primary production to environmental drivers across multiple temporal scales. Sci. Total Environ. 917, 170439. https://doi.org/10.1016/j.scitotenv.2024.170439.

Zhou, B., Cai, W., Zhu, Z., Wang, H., Harrison, S.P., Prentice, I.C., 2025. A general model for the seasonal to decadal dynamics of leaf area. Glob. Change Biol. 31, e70125.

Zhou, Y., Sachs, T., Li, Z., Pang, Y., Xu, J., Kalhori, A., Wille, C., Peng, X., Fu, X., Wu, Y., Wu, L., 2023. Long-term effects of rewetting and drought on GPP in a temperate peatland based on satellite remote sensing data. Sci. Total Environ. 882, 163395. https://doi.org/10.1016/j.scitotenv.2023.163395.

Zong, X., Tian, X., Liu, X., Shu, L., 2024. Drought threat to terrestrial gross primary production exacerbated by wildfires. Commun. Earth Environ. 5, 225. https://doi.org/10.1038/s43247-024-01406-7.